
Electronic Theses and Dissertations, 2004-2019

2017

Timoshenko Beam Viscous Damping Model for Spacecraft Cabling Dynamics

Brandi McPherson
University of Central Florida



Part of the [Space Vehicles Commons](#)

Find similar works at: <https://stars.library.ucf.edu/etd>

University of Central Florida Libraries <http://library.ucf.edu>

This Masters Thesis (Open Access) is brought to you for free and open access by STARS. It has been accepted for inclusion in Electronic Theses and Dissertations, 2004-2019 by an authorized administrator of STARS. For more information, please contact STARS@ucf.edu.

STARS Citation

McPherson, Brandi, "Timoshenko Beam Viscous Damping Model for Spacecraft Cabling Dynamics" (2017). *Electronic Theses and Dissertations, 2004-2019*. 5505.

<https://stars.library.ucf.edu/etd/5505>

TIMOSHENKO BEAM VISCOUS DAMPING MODEL FOR SPACECRAFT
CABLING DYNAMICS

by

BRANDI NICOLE MCPHERSON
B.S. Auburn University, 2015

A thesis submitted in partial fulfillment of the requirements
for the degree of Master of Science
in the Department of Mechanical & Aerospace Engineering
in the College of Engineering and Computer Science
at the University of Central Florida
Orlando, Florida

Summer Term
2017

Major Professor: Jeffrey L. Kauffman

© 2017 Brandi Nicole McPherson

ABSTRACT

Spacecraft data cabling has become an increasingly larger fraction of a spacecraft's dry mass due the growing data and power handling requirements. Data cabling can significantly alter the dynamics of the spacecraft and their effects have been observed during ground-level testing. However, current models do not accurately predict the effects of cables on the structural dynamics of the whole system. For built-up aerospace structures, damping often shows very weak frequency-dependence; current modeling techniques produce highly frequency-dependent damping. Current models utilize Euler-Bernoulli and shear beam formulations; this work investigates the behavior of damping terms within a Timoshenko model. Gaining knowledge of these terms aids in the creation of a frequency-independent viscous damping model which will more accurately predict the damping effects of spacecraft data cabling.

Damping is an important part of the design of aerospace structures. It is responsible for reducing resonant responses as well as aiding in the control of structures. Ideally, accurate damping models should be incorporated into the design process; however, for certain structures, damping models do not accurately predict the system response, and expensive design modifications must be made after testing. Typical damping models such as structural and viscous damping produce frequency-dependent and unrealistic damping. Viscous damping is often in the form of a motion-

or strain-based damping term; more recently, a rotation-based damping term has been added to Euler-Bernoulli beam models to produce approximately frequency-independent damping.

This work incorporates a combination of damping terms along with variable weighting factors into the Timoshenko beam equations. Each of the damping terms is characterized as a specific dissipation mechanism such as motion-, rotation-, and strain-based damping. The damping coefficients, or weighting factors, depend on both transverse shear and rotational inertia parameters, and can be tailored to incorporate the properties of the Timoshenko beam model. By combining terms and investigating damping coefficients, a more realistic frequency-independent damping model can be achieved.

I would like to dedicate this thesis to my parents, who have supported me through my twenty and counting years of education.

ACKNOWLEDGMENTS

This work is supported by the NASA Florida Space Grant Consortium. I would like to thank the FSGC for this fellowship as well as the opportunity to pursue research applicable to the space industry. I would also like to thank my adviser Dr. Jeffrey Kauffman for his encouragement and guidance throughout my graduate career. He has made my time at the University of Central Florida both enjoyable and rewarding, and I am grateful for his patience and valuable input.

I would also like to thank my parents, Billy and Karen McPherson. Their endless love and encouragement has made this process possible. Their support of my decision to continue with graduate school has been very influential on my success. Finally, I would like to thank my friends for their continual support. The past two years would have been vastly different without their comic relief and necessary distractions.

TABLE OF CONTENTS

LIST OF FIGURES	x
LIST OF TABLES	xii
CHAPTER 1 : INTRODUCTION	1
1.1 Motivation	2
1.2 New Approach	3
1.3 Goal of Current Research	5
CHAPTER 2 : BACKGROUND	8
2.1 Spacecraft Data Cabling	8
2.2 Current Modeling Methods and Experimental Testing	12
2.2.1 Damping Models	15
2.3 Timoshenko Beam Model	18
CHAPTER 3 : METHODOLOGY	20
3.1 Undamped Timoshenko Beam	20

3.1.1	Method 1: Galerkin’s Method of Weighted Residuals	21
3.1.2	Method 2: Energy Method	24
3.2	Damped Timoshenko Beam.....	26
3.2.1	Method 1: Motion-, Strain-, and Rotation-Based Damping Terms	26
3.2.2	Method 2: Additional Damping Terms.....	28
CHAPTER 4 : DATA ANALYSIS		30
4.1	Finite Element Code Implementation	30
4.2	Model Validation	33
4.3	Frequency Regimes	35
4.4	Damping Plots	37
4.5	Beam Deformation.....	48
CHAPTER 5 : CONCLUSION		53
5.1	Damping Results	53
5.2	Future Work	55
APPENDIX A : MATLAB CODE FOR BEAM NATURAL FREQUENCIES FEM		57
APPENDIX B : MATLAB CODE FOR BEAM DAMPING FEM		62
APPENDIX C : MATLAB CODE FOR BEAM DEFORMATION		70

LIST OF REFERENCES 76

LIST OF FIGURES

Figure 1.1	Frequency-dependent damping	6
Figure 1.2	Spacecraft cable experimental data	6
Figure 2.1	Spacecraft cable fabrication techniques	10
Figure 2.2	AFRL XSS-11 spacecraft bus structure	11
Figure 2.3	Detailed spacecraft data cabling	11
Figure 2.4	Cable natural frequency test results	15
Figure 2.5	Modal damping values for a shear beam geometric-based damping model ...	18
Figure 4.1	Abaqus model validation for Euler-Bernoulli region	34
Figure 4.2	Abaqus model validation for Timoshenko region	34
Figure 4.3	Surface plots of natural frequencies with varying R and S	36
Figure 4.4	1 st and 40 th mode natural frequencies, 2D view	37
Figure 4.5	R and S case study plot	38
Figure 4.6	Case 1 damping ratios	39
Figure 4.7	Case 2 damping ratios	41

Figure 4.8	Case 3 damping ratios	42
Figure 4.9	Case 4 damping ratios	43
Figure 4.10	Case 2 additional damping terms	46
Figure 4.11	Combinations of damping terms	48
Figure 4.12	Trend lines	49
Figure 4.13	Modes displayed in beam deformation plots	50
Figure 4.14	Case 2 beam deformation, trend 1	51
Figure 4.15	Case 2 beam deformation, trend 2	52

LIST OF TABLES

Table 2.1	Available FE beam models	14
Table 4.1	Damping terms	32
Table 4.2	Damping case study <i>R</i> and <i>S</i> values	38

CHAPTER 1

INTRODUCTION

Due to both the increasing data handling and power requirements of today's spacecraft, data and power cabling are becoming a larger portion of a spacecraft's dry mass. As spacecraft become lighter with advancements in structural materials, the increasing amount of data cabling becomes a larger fraction of the spacecraft's mass. Because these cables are fixed to the spacecraft at various tie-down points, they often interact with the spacecraft's structural dynamics, causing an overestimate of the structure's damping. Current models fail to reproduce this observed effect. Existing methods only incorporate the effects of cabling after ground testing, as opposed to during the design phase. To reduce the need for expensive design modifications, it is of interest to develop a spacecraft structural dynamics model in the time-domain that includes the frequency-independent damping effects of the data cabling as observed in testing [1]. A more accurate model will assist in the development of a highly predictable and reliable structure while also optimizing system functionality and accuracy of finite element models.

1.1 Motivation

Current spacecraft are utilizing more advanced lightweight materials, reducing the mass of the spacecraft; however, the amount of cabling continues to increase due to the expanding power and data handling requirements. Because of the increasing quantity of data and power cabling, cables can account for as much as 30% of the spacecraft's dry mass. With a high dry mass percentage, the cabling harnesses can no longer be neglected in spacecraft dynamics models [2]. Ignoring the effects of the cables can often lead to reduced controller performance, as well as an uncertainty in the structural dynamics of the system [3].

Within the space industry, the term “cabling” refers to any electrical cable used to transfer data or power; however, the term “cable” may cause some confusion when considering typical structural elements. While cables in the traditional sense consist of load bearing elements that only carry tension, spacecraft cabling behaves as a beam element. Data cabling experiences bending, shear, and rotational effects, as well as axial compression and tension; therefore, when modeling spacecraft cabling, beam models are used.

The majority of cable literature focuses on their use as structural elements, such as those in bridges; in spacecraft, data cables are not typically large load bearing structures. Cable harnesses are not generally included in modal analysis of spacecraft except as additional non-structural mass. For non-precision spacecraft, this assumption holds for most frequency ranges; however, for precision spacecraft, system characteristics are often over-estimated in mid- to high-range frequencies [2–4].

Damping is often included in the design of aerospace structures to ensure stability as well as reduce dynamic response; however, more accurate models are needed in the design process. During testing phases, built-up aerospace structures often display damping that displays little frequency-dependence [5–7]. Testing on other structures such as aircraft wings and fuselages has also indicated weak frequency-dependent damping [8]. Viscous damping models are most often used, which result in highly frequency-dependent damping, making such a model inaccurate.

1.2 New Approach

While current finite element cable models can accurately predict the natural frequencies of the system, most utilize structural or proportional damping techniques which provide highly unrealistic and frequency-dependent damping. A more accurate frequency-independent damping model including the effects of data and power cabling can be integrated into the design phase, as opposed to modifying the design after ground testing. These models will result in increased accuracy in system prediction by improving structural dynamic and finite element models.

Spacecraft cabling harnesses are customized to fit the needs of the mission itself. Wires and cable harnesses span a wide range of designs and include manufacturing methods such as twisting, bundling, and pairing [3]. Shear deformation is often observed in cable dynamics; therefore, Euler-Bernoulli and Rayleigh beam models, which only account for bending stiffness and rotational effects respectively, prove insufficient. Current finite element cable models include shear beam theory, which allows for shear deformation. Such models provide accurate frequency analysis

while also capturing the effects of damping to some extent; however, these models generally over-predict the system response [9].

Growing data requirements produces an increasing number of cables; as the cables are bundled and zip-tied together, thick, short segments are formed, much like beams modeled using Timoshenko theory. Timoshenko beam theory allows for both the effects of shear deformation and rotational inertia. A wide variety of damping models exists for use with Timoshenko beams and apply to shear beam theory when ignoring rotational inertia effects. The most common approach, the structural damping model, incorporates both strain- and shear-based damping terms. While some damping models produced as many as 14 damping terms, the majority of these result in zero damping [10].

Other model types include viscous damping. Here, a combination of terms proportional to both the mass and stiffness are often used as damping values, as well as motion- and strain-based terms. While this method proves to be mathematically convenient, the results usually indicate frequency-dependent damping. However, some models have successfully produced frequency-independent damping in an Euler-Bernoulli beam model through the addition of a geometric-based damping term [5, 6]. This same damping term was extended to both shear and Timoshenko beams [1, 11]. While these models did not show frequency-independence for a broad range, the rotation-based damping term did provide less frequency-independence in the bending regime for the shear beam. In addition, the characterization of damping terms as motion-, strain-, or rotation-based is useful in further time-domain modeling methods.

1.3 Goal of Current Research

This work will investigate a damping model for spacecraft cables by including viscous damping terms to the Timoshenko beam equations of motion; the behavior of rotation-based damping and characterization of additional terms is of most interest. Each damping term will be studied individually to determine its effects on the system. This work will also investigate an ideal combination of damping terms, as well as determine damping coefficients, required to produce a more frequency-independent damping model. Because Timoshenko beams include the effects of both transverse shear and rotational inertia, it is of importance to define the damping coefficients in terms of these parameters. Previous work has included motion- and strain-based damping terms to shear and Timoshenko beam equations. Damping ratios exhibited an increase with mode number, similar to Figure 1.1; however, when compared with tested values, these models produce unrealistic damping results [9]. Figure 1.2 displays normalized damping ratios for 100 spacecraft cables. While variation between cables exists, damping ratios indicate only a slight frequency-dependence, decreasing by approximately 20%.

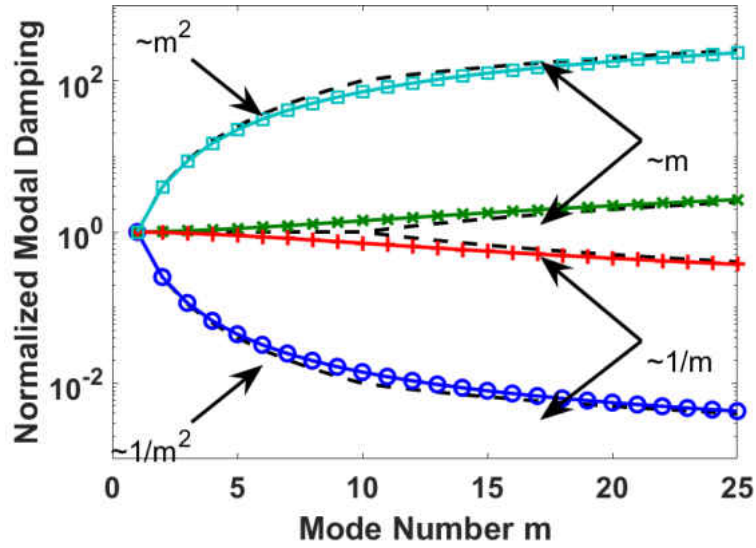


Figure 1.1: Motion- and strain-based damping terms produced frequency-dependent damping in a shear beam model. Adapted from [11].

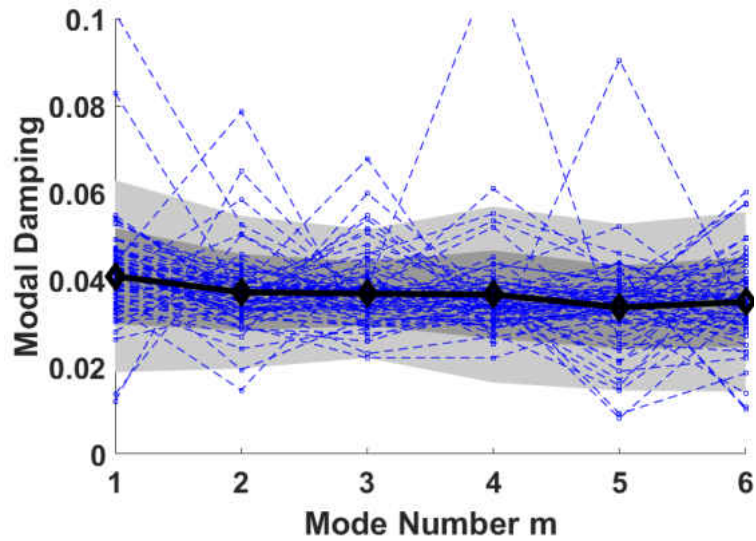


Figure 1.2: Experimental data for over 100 spacecraft cables. Modal damping ratios decrease approximately 20%. Adapted from [11].

In addition to creating a more realistic time-domain damping model, this work will characterize individual damping terms as physical dissipation mechanisms. Viscous damping terms often include motion- and strain-based damping; these terms are derived from a force proportional to the velocity and a moment proportional to beam curvature rate of change. The terms correspond to mass- and stiffness-proportional damping, respectively, but produce modal damping that varies linearly with frequency. This work will introduce new damping terms, and an understanding of the dissipation mechanism they represent will be useful to future damping models.

Following the introduction in Chapter 1, the remainder of this thesis is organized into 4 chapters. Chapter 2 provides a survey of available literature on spacecraft data cabling and damping models. In addition, spacecraft cabling manufacturing techniques and preexisting experimental data are addressed. Chapter 3 includes model development and methodology. This chapter provides the necessary framework used in the analysis section. Results and analysis are discussed in Chapter 4. Various plots and tables representing Timoshenko damping are presented in this chapter. Final comments, conclusions, and future work are addressed in Chapter 5.

CHAPTER 2

BACKGROUND

Previous experimental testing and literature has indicated a need for more accurate predictions of the effects of data cabling on the dynamics of a spacecraft. Before a model can be created, a brief literature survey of spacecraft wiring is conducted, including uses, fabrication, connection methods, and testing. Current modeling techniques are also investigated. Pre-existing models are presented in the following sections and include Euler-Bernoulli beam theory and shear beam theory with structural and proportional damping terms. Finally, existing Timoshenko beam finite elements models are explored.

2.1 Spacecraft Data Cabling

With increasing power and data handling requirements on spacecraft, the quantity of electrical components needed continues to rise. While the total mass of structures such as satellites decreases with advancements in lightweight materials, data and power cabling has become a larger fraction of the total spacecraft dry mass [2]. Data and power cabling can account for as much as 4-30% of a spacecraft's dry mass for some designs [3, 4, 9, 11, 12]. Because of the higher mass fraction, the effects of the wiring on inertial properties and structural dynamics of the spacecraft can no longer

be neglected. System characteristics could be overestimated at mid- to high-range frequencies, reducing controller performance and leading to uncertainty in the system [2, 3].

Existing literature focuses on cabling as a means of a load-bearing element, for example, cables used in cable-stay bridges; however, the data and power cabling used in spacecraft often bear very little load making the information in such literature irrelevant to the problem under investigation. The effect of cables on structural dynamics is not typically modeled in the design phase; cables are usually only included as non-structural mass. For non-precision spacecraft, this assumption holds for most frequency ranges. For light weight, precision spacecraft, low-range frequency system data can be accurately predicted, but mid- to high-range can be altered by cable damping. In one particular study, 96 accelerometers were fixed to a wind turbine blade. After modal damping ratios were calculated, all but 12 of the accelerometers were removed; while the first three mode shapes were not affected, the modal damping ratios decreased by 36%. The cables had caused an overestimate in the original damping ratios, indicating the need for a model including the effects of cable harnesses. For most cases, the influence of cable harnesses are observed during spacecraft ground-testing; for deployable, precision spacecraft, an accurate structural model becomes even more important due to the challenges in simulating microgravity environments during systems testing [2–4].

Because spacecraft are unique, a range of standard cabling fabrication and attachment methods exist. Guidelines set by the European Space Agency, U.S. Department of Defense, NASA, and the Society of Automotive Engineers provide some insight into tie-down spacing as well as harness construction, but no uniform standard exists which addresses the impact of these harnesses on the

structural dynamics [2,3,13–15]; cable attachment most often depends on personal experience [3]. Much research has been conducted on spacecraft cables at the U.S. Air Force Research Laboratory (AFRL), Space Vehicles Directorate, in order to characterize different cabling techniques [2, 3]. In a survey conducted by authors Ardelean et al. and Goodding et al., the most common cable type for space applications was developed from MIL-SPEC, Teflon-coated wire and ranged from 14 to 30 American wire gauge in size. The cabling is formed by twisting, stitching, and braiding pairs of wires to reduce electromagnetic interference [2, 3]. The cables, between 10-30 twisted pairs, are often wrapped with Kapton tape and bundled together with zip-tie connections. These steps are displayed in Figure 2.1. The groups of cables, Figure 2.3, are tied or bonded to a host or bus structure with a tab or wiring harness [2, 4]. Figure 2.2 shows a spacecraft bus including wiring harnesses during final integration at the AFRL and represents a typical quantity of cables on a non-precision spacecraft [2].

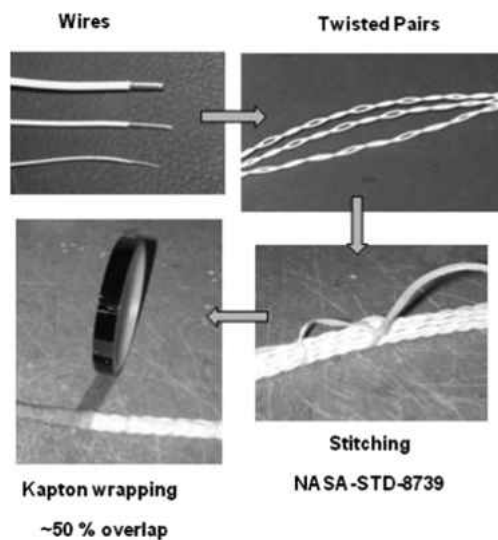


Figure 2.1: Typical spacecraft cable manufacturing techniques. Cables begin as individual wires that are twisted, stitched, and wrapped to create groups of cables.

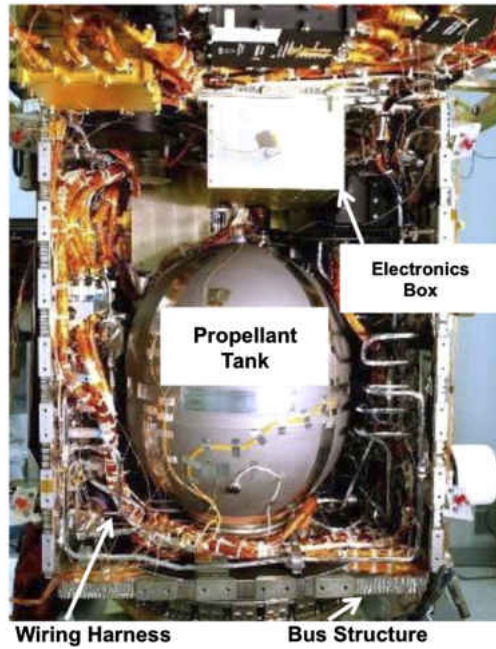
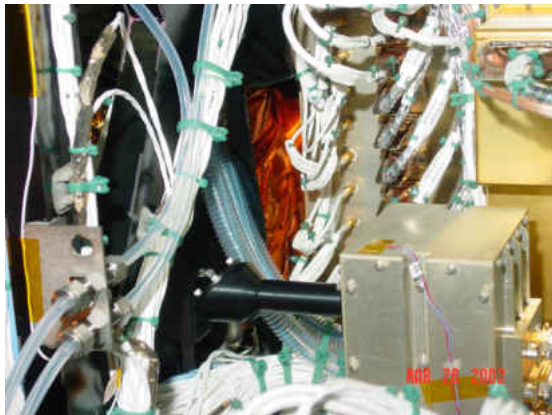


Figure 2.2: AFRL XSS-11 spacecraft bus structure during final integration.



(a) Cabling detail with close-up of zip-tie connections.



(b) Data cabling attached to various tie-down points.

Figure 2.3: Detailed view of spacecraft data cabling. Cables are often zip-tied together and attached to various tie-down points on the bus structure.

2.2 Current Modeling Methods and Experimental Testing

In order to understand the effects that cables play on the dynamics of a structure, both the cables and their attachment methods should be modeled [4]. Existing models assume cables to act as uniform, linear beams. Many beam models exist, as displayed in Table 2.1. The four models presented are readily available in standard finite element software [9]. In an effort to determine which model most accurately depicts cable dynamics, experimental modal analysis was used to extract modal frequencies as well as modal damping ratios and cable material parameters. The modal frequencies were compared to analytical solutions using Euler-Bernoulli and shear beam models [2–4, 9, 12, 16, 17].

Experimental testing on spacecraft cables has been conducted to determine cable properties such as Young's modulus, shear modulus, moment of inertia, estimated cable diameter, and effective mass. Axial tests as well as lateral tests were conducted. These tests were also used to determine modal parameters, such as modal frequency and modal damping ratio.

Axial test methods were used to determine the apparent Young's modulus of a group of cables [2, 3, 12, 17]. Two studies used test specimens made of MIL-SPEC, Teflon coated wires wrapped in Kapton. Results indicated a variation in Young's modulus between 3 – 10 GPa which the authors determined was due to variation in manufacturing [2, 3].

Lateral test methods were used primarily to determine properties for a shear beam model. This test method was also used to extract modal parameters, such as frequency and damping ratios, from frequency response functions (FRF). FRFs revealed that cables produced natural frequencies that

followed a quadratic relationship relative to mode number. When compared to analytical solutions, these natural frequencies were close to those derived with an Euler-Bernoulli beam model for low-frequency modes [12, 16, 17]. However, the experimental frequencies and analytical solutions diverged with increasing mode number, indicating Euler-Bernoulli beam models should only be used for analysis of lower frequency modes [2, 3, 9].

Some studies compared experimental frequencies to analytical solutions using a shear beam model, as opposed to a simple Euler-Bernoulli beam. Shear beam models can be derived from the Timoshenko beam equations by ignoring the effects of rotational inertia, but leaving the transverse shear term [4]. In studies conducted by authors Goodding et al., lateral test methods as well as parameter estimation algorithms confirmed that cable modal frequencies are more accurately represented across a broader range using a shear beam model [3, 17]. Other experimental results indicated a change in cable properties when determined from analysis of the cables only versus a cabled structure [2]. In this case, a shear beam model was then used. Shear beam analysis determined that Euler-Bernoulli models are best suited for lower frequency modes and cables with a high beam slenderness ratio. Figure 2.4 shows modal frequencies from both shear and Euler-Bernoulli beam models. Because cables often exhibit both bending stiffness and shear stiffness, Euler-Bernoulli models were insufficient and over-predicted the modal frequencies [9].

In addition to modal frequencies and cable parameters, cable modal damping was also of interest. Most experimental data resulted in an over-prediction of cable modal damping. Goodding et al. found that cable modal damping was as much as 4% of critical damping; the addition of cable effects in models would reduce the overall resonant response of the system [3]. Other modeling ap-

proaches used an average structural damping value, determined from cable tests [4]. For this case, constant modal damping was assumed; however, model results often produced a low 1st modal damping value with increasing error. At higher modal frequencies, the cable acted as a damper, affecting the overall system frequency. Other works agreed with the dissipative effects of cables, and observed modal damping an order of magnitude higher for a cabled structure than an un-cabled base [9]. A lumped-mass model was used, but was unable to capture the effects of damping and often overestimated the response of the system. Results indicated that a shear beam model could better capture the apparent damping, but still with some over-prediction.

Table 2.1: Categorization of finite element beam models adapted from [9]. These models are used in standard commercial finite element programs.

Rotational inertia allowed?	Shear deformation allowed?	
	No	Yes
No	Euler-Bernoulli	Shear
Yes	Rayleigh	Timoshenko

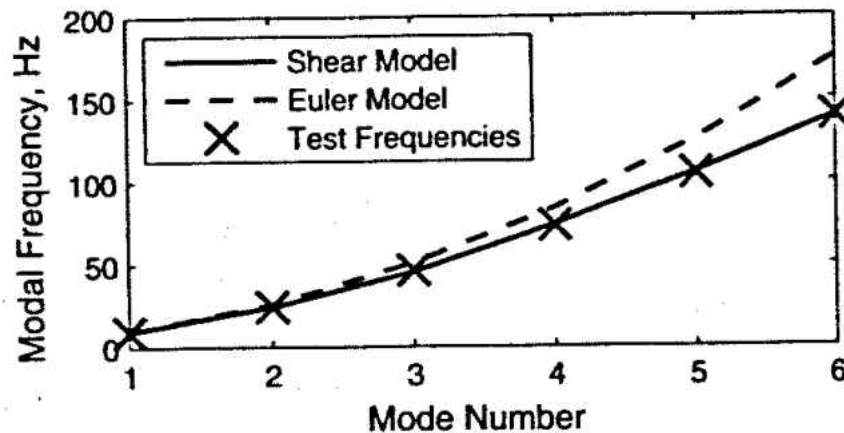


Figure 2.4: Experimental spacecraft cable natural frequency test results compared with Euler-Bernoulli and shear beam model results from [9]. Euler-Bernoulli model errors increase with mode number. Shear beam models display more accurate frequency predictions.

2.2.1 Damping Models

Two of the most common forms of damping are structural damping and viscous damping. Structural damping, or hysteretic damping, utilizes a complex modulus, and its calculation is independent of frequency [18]. Hysteretic damping is most commonly used for analysis of the steady-state response of a system. Viscous damping models are usually linear and proportional to the system state velocities. Created by Rayleigh for mathematical convenience, a viscous damping matrix is often proportional to both the mass and stiffness matrix [19]. Though mathematically convenient, viscous damping provides highly frequency-dependent damping. Generally, damping models in systems are proportional to velocity, and increase with frequency; however, more recently a con-

cept of frequency-independent damping has been introduced. This is due to the observed damping results in experimental testing of aircraft wings and fuselages and other lightly-damped aerospace structures [5, 8].

A variety of damping models exist and have been investigated for use with a large majority of beam types. For example, a combination of viscous and hysteretic damping terms were considered in an Euler-Bernoulli beam model and compared to experimental results by authors Banks et al. [20]. In this particular case an “air damping” model was used in combination with a spatial hysteretic damping mechanism that interprets transverse beam vibration. A similar concept of combining structural and viscous terms was applied to a Timoshenko beam model [10]. In this case, as many as 14 viscous and structural damping terms were considered; however, in a more practical application, only a few would result in nonzero terms. While neither of the two cases mentioned above produce frequency-independent damping, the results were successful in investigating new damping terms and creating a more convenient computer model.

Frequency-independent damping has been achieved for a simply supported Euler-Bernoulli beam model through the addition of a viscous “geometric-based” damping term [5]. While a common approach to viscous damping includes a motion- and strain-based term (a lateral force and moment, respectively) the additional geometric- or rotation-based damping term is an internal shear force, proportional to the slope time rate of change. Where motion-based damping decreases with the square of the mode number, and strain-based damping increases, rotation-based damping is nominally independent of mode number and natural frequency. A similar study was conducted for other boundary conditions [6]. Clamped-clamped boundary conditions produced strong

frequency-dependent damping in the first 6 modes, as normalized damping ratios increase by 45%; however, the difference in damping decreases to less than 10% for the remaining 44 modes. A cantilevered beam displays a similar trend, except from modes 1 to 7, the damping ratios increase; the difference between the remaining modes is again less than 10%.

The concept of a geometric-based damping term has been applied to both shear and Timoshenko beams as well with applications to spacecraft data cabling. The shear beam model included two time-based viscous damping terms dependent on the change in beam shear angles and center-line bending [11]. Two parameters were determined to represent the damping for both shear and bending angles. Various ratios of shear to bending parameters were tested, displayed in Figure 2.5. Two regimes of damping can be seen, one dominated by bending and the other dominated by shear. When a ratio of 1/2 is used, represented by $x's$ in the figure, modal damping was approximately constant in the bending regime. The same model was applied to Timoshenko beams, with the assumption that rotary inertia terms would add some degree of frequency-independence [1]. Results indicated that when effects of rotary inertia and shear deformation were low, much like in an Euler-Bernoulli beam model, the rotation-based damping term provided approximately constant modal damping across the first 50 modes. As the effects of rotary inertia and shear parameters increased, the rotation-based damping term produced modal damping much like results produced with typical motion- and strain-based terms; however, the rate at which the modal damping increased or decreased was much slower. Some modes also produced significantly less damping than others, approximately zero at times.

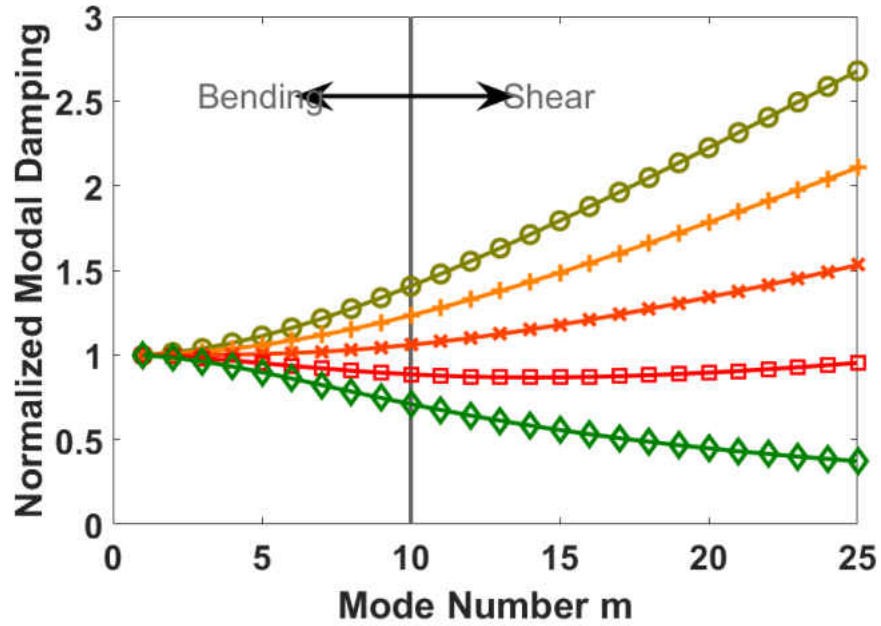


Figure 2.5: Modal damping values for a shear beam geometric-based damping model adapted from [11]. Modal damping ratios indicate a transition between bending- and shear-dominated regimes.

2.3 Timoshenko Beam Model

Euler-Bernoulli beam theory is best applied to thin, slender beams while Timoshenko beam theory most often applies to short, thick beams and composite structures where the cross-sectional area is larger in comparison to the beam length [21–24]. For lower vibration modes, neglecting the effects of rotary inertia and shear deformation is a common assumption; however, for higher modes of vibration, Euler-Bernoulli theory over-predicts frequency responses. Timoshenko beam theory

includes the effects of both rotary inertia and shear deformation, making it an acceptable model for higher order modes [25–27].

A common problem experienced in simple Timoshenko beam finite element models is shear-locking [21, 23, 24]. Shear-locking can occur when the shape functions are created using linear interpolation functions. A number of Timoshenko beam finite element formulations have been investigated. Most can be described as using simple or complex elements. A simple element has two degrees of freedom at two nodes, and a complex element has more than four degrees of freedom. Authors Thomas et al. created a 6-DOF and 8-DOF Timoshenko model that incorporated all possible boundary conditions using cubic polynomial expansions for displacement [25, 26]. Authors Friedman and Kosmatka developed a two-node finite element model that accurately predicts beam displacement and is absent of the shear-locking problem [23, 24]. The shape functions were developed from a cubic polynomial for translational displacement and a quadratic polynomial for rotational displacement. The finite element formulation was developed using Hamilton's principle. Other works have used a cubic polynomial for displacement and linear expansion for shear rotation [21]. This particular model also eliminated the problem of shear-locking and lead to decoupling of the bending and shear deformation.

CHAPTER 3 METHODOLOGY

To develop a finite element formulation for a Timoshenko beam, the undamped equations of motion, including both the effects of rotary inertia and first-order transverse shear are considered. From a weak form of these equations, a finite element model can be derived. The preferred method in deriving the mass and stiffness matrices is the Galerkin method of weighted residuals combined with integration by parts. The second method used considers the energy of the system. The damped equations of motion are considered separately, using only method of weighted residuals to determine the finite element formulation.

3.1 Undamped Timoshenko Beam

To understand the process of developing and implementing a finite element model, the undamped Timoshenko beam equations of motion are first examined. In Equation 3.2, w is the beam transverse displacement, φ is the beam centerline rotation, and q is a distributed lateral load. The slope of the beam involves contributions from the centerline rotation and shear deformation β

$$w' = \beta + \varphi \tag{3.1}$$

The terms EI and κAG represent the beam flexural stiffness and shear stiffness, respectively. Beam density is represented by ρ , and I and A are the beam moment of inertia and area. Time derivatives are indicated by $(\dot{})$ and spatial derivatives are indicated by $()'$. For the initial analysis, the beam is treated as simply-supported and isotropic, requiring both displacement and bending moment to be zero at the beam endpoints and constant properties throughout the beam length.

$$\begin{aligned} -\rho A \ddot{w} + \kappa AG(w'' - \varphi') + q &= 0 \\ -\rho I \ddot{\varphi} + EI\varphi'' + \kappa AG(w' - \varphi) &= 0 \end{aligned} \tag{3.2}$$

3.1.1 Method 1: Galerkin's Method of Weighted Residuals

The first method used in solving the beam differential equations of motion is Galerkin's method of weighted residuals. Beginning with the undamped Timoshenko beam Equations 3.2, and multiplying the set of equations by weighting functions, $w(x)$ and $\varphi(x)$, leads to a weak form of the Timoshenko beam. Applying Galerkin's method, the new set of equations is integrated over the beam length L , resulting in the following integral and additional integration by parts terms

$$\begin{aligned} \int_0^L (w\rho A \ddot{w} + w'\kappa AGw' - w'\kappa AG\varphi - wq)dx + \kappa AG(w\varphi - ww')\Big|_0^L &= 0 \\ \int_0^L (\varphi\rho I \ddot{\varphi} + \varphi'EI\varphi' - \varphi\kappa AGw' + \varphi\kappa AG\varphi)dx - EI\varphi\varphi'\Big|_0^L &= 0 \end{aligned} \tag{3.3}$$

In matrix form,

$$\int_0^L \left(\begin{bmatrix} w \\ \varphi \end{bmatrix}^T \begin{bmatrix} \rho A & 0 \\ 0 & \rho I \end{bmatrix} \begin{bmatrix} \ddot{w} \\ \dot{\varphi} \end{bmatrix} + \begin{bmatrix} \varphi' \\ \varphi - w' \end{bmatrix}^T \begin{bmatrix} EI & 0 \\ 0 & \kappa AG \end{bmatrix} \begin{bmatrix} \varphi' \\ \varphi - w' \end{bmatrix} + \begin{bmatrix} w \\ \varphi \end{bmatrix}^T \begin{bmatrix} q \\ 0 \end{bmatrix} \right) dx \quad (3.4)$$

$$+ \left(\begin{bmatrix} w \\ \varphi \end{bmatrix}^T \begin{bmatrix} 0 & \kappa AG \\ 0 & 0 \end{bmatrix} \begin{bmatrix} w \\ \varphi \end{bmatrix} - \begin{bmatrix} w \\ \varphi \end{bmatrix}^T \begin{bmatrix} \kappa AG & 0 \\ 0 & EI \end{bmatrix} \begin{bmatrix} w' \\ \varphi' \end{bmatrix} \right) \Big|_0^L = 0$$

To develop a finite element formulation the coordinates w and φ are rewritten with a set of shape functions. This work uses a pre-existing approach found in an article by Kosmatka et al [24], interpolating w using a cubic polynomial and a quadratic for φ . Using this solution, the shear-locking problem is avoided. Now, the coordinates can be written as

$$w = [N_w] \{ \delta \} \quad (3.5)$$

$$\varphi = [N_\varphi] \{ \delta \}$$

where $\{ \delta \}$ is a set of nodal displacements and rotations

$$\{ \delta \} = \begin{bmatrix} w_A & \varphi_A & w_B & \varphi_B \end{bmatrix}^T \quad (3.6)$$

The shape functions are

$$[N_w]^T = \begin{bmatrix} \frac{1}{1+\phi} \left\{ 2\left(\frac{x}{L_{el}}\right)^3 - 3\left(\frac{x}{L_{el}}\right)^2 - \phi \frac{x}{L_{el}} + 1 + \phi \right\} \\ \frac{L_{el}}{1+\phi} \left\{ \left(\frac{x}{L_{el}}\right)^3 - \left(2 + \frac{\phi}{2}\right)\left(\frac{x}{L_{el}}\right)^2 + \left(1 + \frac{\phi}{2}\right)\left(\frac{x}{L_{el}}\right) \right\} \\ - \frac{1}{1+\phi} \left\{ 2\left(\frac{x}{L_{el}}\right)^3 - 3\left(\frac{x}{L_{el}}\right)^2 - \phi \frac{x}{L_{el}} \right\} \\ \frac{L_{el}}{1+\phi} \left\{ \left(\frac{x}{L_{el}}\right)^3 - \left(1 - \frac{\phi}{2}\right)\left(\frac{x}{L_{el}}\right)^2 - \left(\frac{\phi}{2}\right)\left(\frac{x}{L_{el}}\right) \right\} \end{bmatrix} \quad (3.7)$$

$$[N_\phi]^T = \begin{bmatrix} \frac{6}{(1+\phi)L_{el}} \left\{ \left(\frac{x}{L_{el}}\right)^2 - \frac{x}{L_{el}} \right\} \\ \frac{1}{1+\phi} \left\{ 3\left(\frac{x}{L_{el}}\right)^2 - (4+\phi)\left(\frac{x}{L_{el}}\right) + 1 + \phi \right\} \\ -\frac{6}{(1+\phi)L_{el}} \left\{ \left(\frac{x}{L_{el}}\right)^2 - \frac{x}{L_{el}} \right\} \\ \frac{1}{1+\phi} \left\{ 3\left(\frac{x}{L_{el}}\right)^2 - (2-\phi)\left(\frac{x}{L_{el}}\right) \right\} \end{bmatrix} \quad (3.8)$$

By inserting the shape functions into Equation 3.4, the equations can now be written as

$$\begin{aligned} \int_0^L \{\delta\} & \left(\begin{bmatrix} [N_w] \\ [N_\phi] \end{bmatrix}^T \begin{bmatrix} \rho A & 0 \\ 0 & \rho I \end{bmatrix} \begin{bmatrix} [N_w] \\ [N_\phi] \end{bmatrix} \right) \{\ddot{\delta}\} \\ & + \begin{bmatrix} [N'_\phi] \\ [N_\phi] - [N'_w] \end{bmatrix}^T \begin{bmatrix} EI & 0 \\ 0 & \kappa AG \end{bmatrix} \begin{bmatrix} [N'_\phi] \\ [N_\phi] - [N'_w] \end{bmatrix} \{\delta\} \\ & + \begin{bmatrix} [N_w] \\ [N_\phi] \end{bmatrix}^T \begin{bmatrix} q \\ 0 \end{bmatrix} \right) dx = 0 \end{aligned} \quad (3.9)$$

From this form, the $\{\ddot{\delta}\}$ and $\{\delta\}$ terms together are grouped together to create the mass and stiffness matrices. The mass matrix is derived from the terms including the second time derivative, while the stiffness matrix comes from terms with no time derivatives.

$$[M] = \int_0^L \begin{bmatrix} [N_w] \\ [N_\phi] \end{bmatrix}^T \begin{bmatrix} \rho A & 0 \\ 0 & \rho I \end{bmatrix} \begin{bmatrix} [N_w] \\ [N_\phi] \end{bmatrix} dx \quad (3.10)$$

$$\begin{aligned}
[K_{new}] = & \int_0^L \begin{bmatrix} [N'_\varphi] \\ [N_\varphi] - [N'_w] \end{bmatrix}^T \begin{bmatrix} EI & 0 \\ 0 & \kappa AG \end{bmatrix} \begin{bmatrix} [N'_\varphi] \\ [N_\varphi] - [N'_w] \end{bmatrix} dx \\
+ & \left(\begin{bmatrix} [w] \\ [\varphi] \end{bmatrix}^T \begin{bmatrix} 0 & \kappa AG \\ 0 & 0 \end{bmatrix} \begin{bmatrix} [w] \\ [\varphi] \end{bmatrix} - \begin{bmatrix} [w] \\ [\varphi] \end{bmatrix}^T \begin{bmatrix} \kappa AG & 0 \\ 0 & EI \end{bmatrix} \begin{bmatrix} [w'] \\ [\varphi'] \end{bmatrix} \right) \Big|_0^L
\end{aligned} \tag{3.11}$$

The integral terms of the mass and stiffness matrices agree with previously accepted matrices. However, the additional integration by parts terms are not negligible for certain boundary conditions, and are out of scope for this analysis.

3.1.2 Method 2: Energy Method

The second approach to developing a finite element model uses the energy method. The Timoshenko beam equations of motion can be derived by substituting the strain, potential, and kinetic energies, as well as the work of external forces into Hamilton's principle [24]. Using an isotropic beam of length L , cross sectional area A , beam transverse displacement w , and beam centerline slope φ , the mass and stiffness matrices are derived.

Strain components of the beam as well as some important material relations are written as follows:

$$\begin{aligned}
 \varepsilon_{xx} &= -y \frac{\partial \varphi}{\partial x} \\
 \gamma_{xy} &= \frac{\partial w}{\partial x} - \varphi \\
 \tau_{xy} &= G \gamma_{xy} \\
 \sigma_x &= E \varepsilon_x \\
 I &= \int_A y^2 dA
 \end{aligned} \tag{3.12}$$

The stiffness matrix can be derived from the strain energy, given as

$$U = \frac{1}{2} \int_0^L \int_A [\boldsymbol{\sigma}]^T [\boldsymbol{\varepsilon}] dA dx \tag{3.13}$$

Using the beam material equations listed in Equation 3.12 and integrating over the cross-sectional area A , the strain energy becomes

$$U = \frac{1}{2} \int_0^L \begin{bmatrix} \frac{\partial \varphi}{\partial x} \\ \frac{\partial w}{\partial x} - \varphi \end{bmatrix}^T \begin{bmatrix} EI & 0 \\ 0 & \kappa AG \end{bmatrix} \begin{bmatrix} \frac{\partial \varphi}{\partial x} \\ \frac{\partial w}{\partial x} - \varphi \end{bmatrix} dx \tag{3.14}$$

The beam kinetic energy is written as

$$T = \frac{1}{2} \int_0^L \int_A \rho \left(\left(\frac{\partial u}{\partial t} \right)^2 + \left(\frac{\partial v}{\partial t} \right)^2 + \left(\frac{\partial w}{\partial t} \right)^2 \right) dA dx \tag{3.15}$$

leading to

$$T = \frac{1}{2} \int_0^L \begin{bmatrix} \frac{\partial w}{\partial t} \\ \frac{\partial \varphi}{\partial t} \end{bmatrix}^T \begin{bmatrix} \rho A & 0 \\ 0 & \rho I \end{bmatrix} \begin{bmatrix} \frac{\partial w}{\partial t} \\ \frac{\partial \varphi}{\partial t} \end{bmatrix} dx \tag{3.16}$$

This method results in previously accepted symmetric Timoshenko mass and stiffness matrices, without any residual terms.

3.2 Damped Timoshenko Beam

This work is primarily interested in characterizing damping terms for a Timoshenko beam; understanding the physical dissipative mechanisms associated with each damping term will aid in the creation of a more frequency-independent damping model. Two methods for choosing damping terms are discussed here.

3.2.1 Method 1: Motion-, Strain-, and Rotation-Based Damping Terms

Method 1 uses motion-, strain-, and rotation-based damping terms associated with the shear angle β . The coefficients associated with these terms describe the dissipative mechanism. For example, a term containing α_φ is closely associated with motion of the beam centerline angle; α_β relates to the shear angle. Using the same method as described in the previous sections, we now use the damped Timoshenko beam equations multiplied by the same weighting functions and integrate over the beam length resulting in

$$\begin{aligned}
 & \int_0^L (w\rho A\ddot{w} + w\kappa AG\varphi' + w\alpha_{Mw}\dot{w} + w\alpha_\varphi\dot{\varphi}' - w\alpha_{\kappa\beta}\dot{\varphi}' + w'\kappa AGw' + w'\alpha_{\kappa\beta}\dot{w}')dx = 0 \\
 & \int_0^L (\varphi\rho I\ddot{\varphi} + \varphi'EI\varphi' - \varphi\kappa AGw' + \varphi\kappa AG\varphi + \dot{\varphi}'\alpha_{\kappa\varphi}\varphi' + \varphi\alpha_{Mw}\dot{\varphi} + \varphi\alpha_\beta\dot{\varphi} \\
 & \quad - \varphi\alpha_\beta\dot{w}' - \varphi\alpha_w\dot{w}')dx = 0
 \end{aligned} \tag{3.17}$$

In matrix form

$$\begin{aligned}
& \int_0^L \left(\begin{bmatrix} w \\ \varphi \end{bmatrix}^T \begin{bmatrix} 0 & 0 \\ 0 & -\kappa AG \end{bmatrix} \begin{bmatrix} w \\ \varphi \end{bmatrix} + \begin{bmatrix} w \\ \varphi \end{bmatrix}^T \begin{bmatrix} -\alpha_{Mw} & 0 \\ 0 & -(\alpha_{M\varphi} + \alpha_\beta) \end{bmatrix} \begin{bmatrix} \dot{w} \\ \dot{\varphi} \end{bmatrix} \right. \\
& + \begin{bmatrix} w \\ \varphi \end{bmatrix}^T \begin{bmatrix} -\rho A & 0 \\ 0 & -\rho I \end{bmatrix} \begin{bmatrix} \ddot{w} \\ \ddot{\varphi} \end{bmatrix} + \begin{bmatrix} w \\ \varphi \end{bmatrix}^T \begin{bmatrix} 0 & -\kappa AG \\ \kappa AG & 0 \end{bmatrix} \begin{bmatrix} w' \\ \varphi' \end{bmatrix} + \begin{bmatrix} w \\ \varphi \end{bmatrix}^T \begin{bmatrix} \kappa AG & 0 \\ 0 & EI \end{bmatrix} \begin{bmatrix} w'' \\ \varphi'' \end{bmatrix} \\
& \left. + \begin{bmatrix} w \\ \varphi \end{bmatrix}^T \begin{bmatrix} 0 & (\alpha_\varphi - \alpha_{\kappa\beta}) \\ (\alpha_\beta + \alpha_w) & 0 \end{bmatrix} \begin{bmatrix} \dot{w}' \\ \dot{\varphi}' \end{bmatrix} + \begin{bmatrix} w \\ \varphi \end{bmatrix}^T \begin{bmatrix} \alpha_{\kappa\beta} & 0 \\ 0 & \alpha_{\kappa\varphi} \end{bmatrix} \begin{bmatrix} \dot{w}'' \\ \dot{\varphi}'' \end{bmatrix} \right) dx = 0
\end{aligned} \tag{3.18}$$

Again using the same shape functions and displacement vector we arrive at the finite element formulation. Terms including $\{\dot{\delta}\}$ are grouped together to form the damping matrix

$$\begin{aligned}
[C] = \int_0^L \left(\alpha_{Mw} [N_w]^T [N_w] - (\alpha_\varphi - \alpha_{\kappa\beta}) [N_\varphi]^T [N'_w] + \alpha_{\kappa\beta} [N'_w]^T [N'_w] + \alpha_{EI} [N'_\varphi]^T [N'_\varphi] \right. \\
\left. + (\alpha_{M\varphi} + \alpha_\beta) [N_\varphi]^T [N_\varphi] + (\alpha_\beta + \alpha_w) [N_w]^T [N'_\varphi] \right) dx
\end{aligned} \tag{3.19}$$

Due to the coupling of terms such as $[N_\varphi]^T [N'_w]$ and $[N_w]^T [N'_\varphi]$ from method of weight residuals, the damping matrix is not symmetric. In an effort to create a symmetric damping matrix, the form $.5(A + A^T)$ is used. The term A represents the non-symmetric matrix of interest. This concept is investigated further in the damping analysis section.

3.2.2 Method 2: Additional Damping Terms

Method 2 uses ten terms with variable α parameters. These terms are used to investigate damping mechanisms that may not be considered in method 1, as well as to force a way to categorize dissipative mechanisms that may not be easily recognizable. For example, a term containing \dot{w} can easily be characterized as motion-based damping, but a term containing \dot{w}'''' is more challenging to classify at first glance.

Ten damping terms, including both third- and fourth-order spatial derivatives, were added to the Timoshenko beam equations of motion. Unlike method 1, the damping terms in Equation 3.20 have variable damping coefficients α and the physical dissipative mechanism that corresponds to each is not well known. Method of weighted residuals along with shape functions and the displacement vector were used to determine the mass, stiffness, and damping matrices.

$$\begin{aligned} -\rho A \ddot{w} + \kappa A G (w'' - \phi') + q &= \alpha_1 \dot{w} - \alpha_2 \dot{w}'' + \alpha_3 \dot{w}'''' - \alpha_4 \dot{\phi}' + \alpha_5 \dot{\phi}''' \\ -\rho I \ddot{\phi} + EI \phi'' + \kappa A G (w' - \phi) &= -\alpha_6 \dot{w}' + \alpha_7 \dot{w}''' + \alpha_8 \dot{\phi} - \alpha_9 \dot{\phi}'' + \alpha_{10} \dot{\phi}'''' \end{aligned} \quad (3.20)$$

$$\begin{aligned} \int_0^L (w \rho A \ddot{w} + w' \kappa A G w' - w' \kappa A G \phi - w q + w \alpha_1 \dot{w} - w \alpha_2 \dot{w}'' + w \alpha_3 \dot{w}'''' - w \alpha_4 \dot{\phi}' + w \alpha_5 \dot{\phi}''') dx \\ \int_0^L (\phi \rho I \ddot{\phi} + \phi' EI \phi' - \phi \kappa A G w' + \phi \kappa A G \phi - \phi \alpha_6 \dot{w}' + \phi \alpha_7 \dot{w}''' + \phi \alpha_8 \dot{\phi} - \phi \alpha_9 \dot{\phi}'' + \phi \alpha_{10} \dot{\phi}''') dx \end{aligned} \quad (3.21)$$

The mass matrix agrees with pre-existing Timoshenko beam finite element formulations. The stiffness matrix, after performing integration by parts and ignoring the residual terms, matches those in existing literature. The resulting damping matrix can be divided into 10 separate damping

terms, with 10 different coefficients, before integrating by parts. These terms will be categorized as motion-, strain-, and rotation-based damping, and their behavior will be analyzed in further chapters.

CHAPTER 4

DATA ANALYSIS

A finite element model is implemented into Matlab using the equations derived in Chapter 3. To characterize the damping terms as physical dissipative mechanisms, each of the ten damping terms from method 2 were considered separately in the code; by studying the terms individually, the effects of motion-, strain-, and rotation-based damping can be more easily identified. Understanding individual damping terms is a necessary step in developing a more frequency-independent damping model. The natural frequencies, especially those of higher modes, and modal damping ratios are calculated for various transverse shear and rotational inertia parameters. To obtain a better visual representation of the effects of each damping term, normalized damping ratios, the mode shapes, beam deformation, and shear deformation are plotted.

4.1 Finite Element Code Implementation

Using the stiffness and mass matrices derived via method of weighted residuals, the model accounts for a user defined number of elements, beam length, ρA , EI , and R and S values. The two parameters, R and S , are defined as the effect of rotary inertia and effect of transverse shear, respectively, where $R = \rho I / \rho A$ and $S = \kappa AG / EI$. The units for R are length squared, while the units for

S are the inverse length squared. The finite element model supports various boundary conditions, such as fixed-fixed, fixed-free, fixed-pinned, and pinned-pinned. For the purposes of this analysis, a simply-supported uniform beam of length 10 meters is examined, with ρA and EI defined as 1 and the number of elements as 50. The length of each element is determined by dividing the beam length by the total number of elements.

The derivatives of the shape functions are first calculated. First through fourth order spatial derivatives with respect to x for both $[N_w]$ and $[N_\phi]$ are stored separately. Because the shape functions are used to calculate the local mass, stiffness, and damping matrices, the length of the element should be used instead of the entire length of the beam; all instances of L are changed to L_{el} . As seen in Equations 3.10 and 3.11, different combinations of shape functions and their derivatives are multiplied and integrated over the length of the element. For easier naming convention, the integrals are written as follows: $\int_0^{L_{el}} [N_w]^T [N_w] dx = N_{w_0w_0}$, $\int_0^{L_{el}} [N_w]^T [N'_\phi] dx = N_{w_0t_1}$, etc. Note that these terms do not include the coefficients such as EI or ρA , but are incorporated into the next section of the code.

Next, the local mass, stiffness, and damping matrices are initialized and constructed using Equations 3.10 and 3.11. Through the matrix multiplication and integrals previously defined and substitution of R and S , the formulas implemented into Matlab are as follows, resulting in a symmetric mass and stiffness matrix:

$$\begin{aligned}
 k_{mat} &= EI * (N_{t_1t_1} + S * N_{w_1w_1} + S * N_{t_0t_0} - S * N_{w_1t_0} - S * N_{t_0w_1}) \\
 m_{mat} &= \rho A * (N_{w_0w_0} + R * N_{t_0t_0})
 \end{aligned}
 \tag{4.1}$$

For each of the 10 damping terms in Equation 3.20 a separate $[c_i]$ local damping matrix is created. Matrices $[c_3]$, $[c_5]$, and $[c_{10}]$ are not considered for the remainder of the analysis. These terms include third- and fourth-order spatial derivatives of $[N_\phi]$ and $[N_w]$. Because these matrices reduce to zero, no damping is achieved. The remaining damping terms are summarized in Table 4.1. The terms have been categorized as motion-, strain-, or rotation-based damping by the Euler-Bernoulli damping plots. This is discussed in further detail in a later section.

Table 4.1: Damping terms used within the FE code. Terms were categorized based on Euler-Bernoulli modal damping results presented in a further section.

Motion	Strain	Rotation
$[c_1] = N_{w_0 w_0}$	$[c_7] = N_{t_0 w_3}$	$[c_2] = N_{w_0 w_2}$
	$[c_9] = N_{t_0 t_2}$	$[c_4] = N_{w_0 t_1}$
		$[c_6] = N_{t_0 w_1}$
		$[c_8] = N_{t_0 t_0}$

With the completion of the local element matrices, the global matrices are constructed by running a for loop n times, where n is defined as the number of elements. Boundary conditions are applied to the global matrices, which are an initial size of $2n + 2$. For a simply-supported beam, the first and second to last row and column of each of the mass, stiffness, and damping matrices should equal zero; this corresponds to the zero displacement condition at $x = 0$ and $x = L$ due to the pin connections.

The beam natural frequencies and damping ratios are calculated using the generalized eigenvalue problem of the form $Ax_i = \lambda_i Bx_i$ in Matlab where

$$A = \begin{bmatrix} C & K \\ -I & 0 \end{bmatrix} \quad B = \begin{bmatrix} M & 0 \\ 0 & I \end{bmatrix} \quad (4.2)$$

and I is the identity matrix. The eigenvalues are sorted in ascending order, and the natural frequencies are calculated as $\omega_i = |\lambda_i|$. The damping ratio is defined as $\zeta_i = \text{Re}(\lambda_i)/\omega_i$. Because the eigenvalues occur in complex conjugates, it is only necessary to list every other value.

4.2 Model Validation

To validate the finite element model created in Matlab, natural frequency results were compared to those developed with an Abaqus model. The Abaqus model uses 500 B21 beam elements; beam elements account for all deformation types that occur in Timoshenko models. Multiple cases were studied, with varying R and S values and beam thicknesses. For the purposes of this analysis, two cases are displayed which represent an approximate Euler-Bernoulli and Timoshenko model.

Percent error for the first five natural frequencies was calculated, using the Matlab code as the accepted values ($\% \text{ error} = \frac{\omega_{\text{Abaqus}} - \omega_{\text{Matlab}}}{\omega_{\text{Matlab}}} * 100$). An aluminum beam with properties $E = 68.9\text{E}3 \text{ MPa}$, $\nu = .333$, $L = 10 \text{ mm}$, $\rho = 2.7\text{E}-9 \text{ tonne/mm}^3$, $G = 26.6\text{E}3 \text{ MPa}$ and $w = .2 \text{ mm}$ was used for the analysis.

The first case is more representative of an Euler-Bernoulli beam, with $t = .1 \text{ mm}$, $R = 8.33\text{E}-4 \text{ mm}^2$ and $S = 3.85\text{E}2 \text{ mm}^{-2}$. Figure 4.1 displays percent error results for the first five

modes. Percent error remains on the order of magnitude of 1E-3, indicating high accuracy between Matlab and Abaqus models.

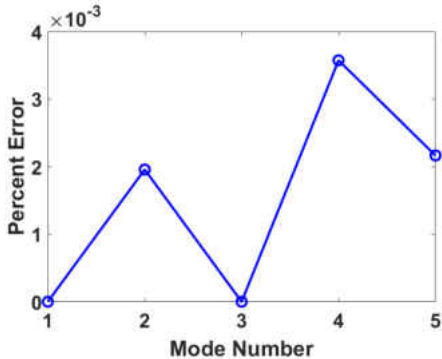


Figure 4.1: Percent error between Matlab and Abaqus natural frequencies for $R = 8.33E-4 mm^2$ and $S = 3.85E2 mm^{-2}$. Very small percent error in Euler-Bernoulli range.

Figure 4.2 displays results for a beam of the same material properties, but differing thickness and R and S parameters ($t = 2 mm$, $R = 3.33E-1 mm^2$, and $S = 9.63E-1 mm^{-2}$). Percent error remains very small, less than 0.1% for the first five modes, validating the finite element formulation for larger ranges of R and S .

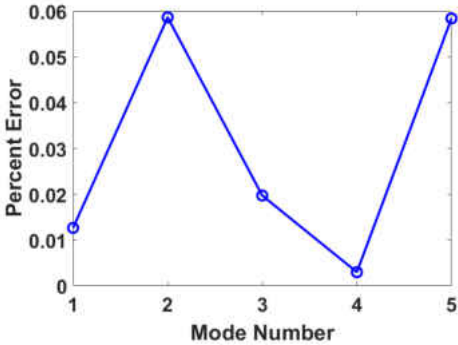


Figure 4.2: Percent error between Matlab and Abaqus natural frequencies for $R = 3.33E-1 mm^2$ and $S = 9.63E-1 mm^{-2}$. Small percent error indicates model validation.

4.3 Frequency Regimes

This work is primarily interested in viscous damping in Timoshenko beams. Before damping coefficients can be determined, it is necessary to define the set of parameters that define a Timoshenko beam. Using the previously defined terms R and S , different regions of beam types are shown by calculating natural frequencies. Using a range of R and S values from $1E-5$ to $1E5$ on a logarithmic scale, natural frequencies for a simply supported beam were plotted; because previous models fail to predict accurate spacecraft dynamics in mid- to high-range frequency modes, the 1st, 5th, 15th, and 40th were examined. The set of R and S values used in the remainder of this analysis are taken from the higher mode plots. Four beam models can be represented by the shear and rotational parameters: Euler-Bernoulli, Timoshenko, Rayleigh, and shear. A larger S value indicates a lower shear effect. Small R , approximately zero, combined with high S define the Euler-Bernoulli regime. Low S combined with low R define the shear regime, meaning the beam will deform in shear. High R and S values indicate the Rayleigh regime. Low S and high R indicate Timoshenko. Each frequency plot displays a transition area between the four beam models.

The R and S values for an Euler-Bernoulli case and multiple Timoshenko cases are used in further damping calculations. Figure 4.3 displays a clear plateau in the Euler-Bernoulli range with downward slopes towards the other three beam model regions. The Euler-Bernoulli area decreases in size with increasing mode number, while the remaining regions increase.

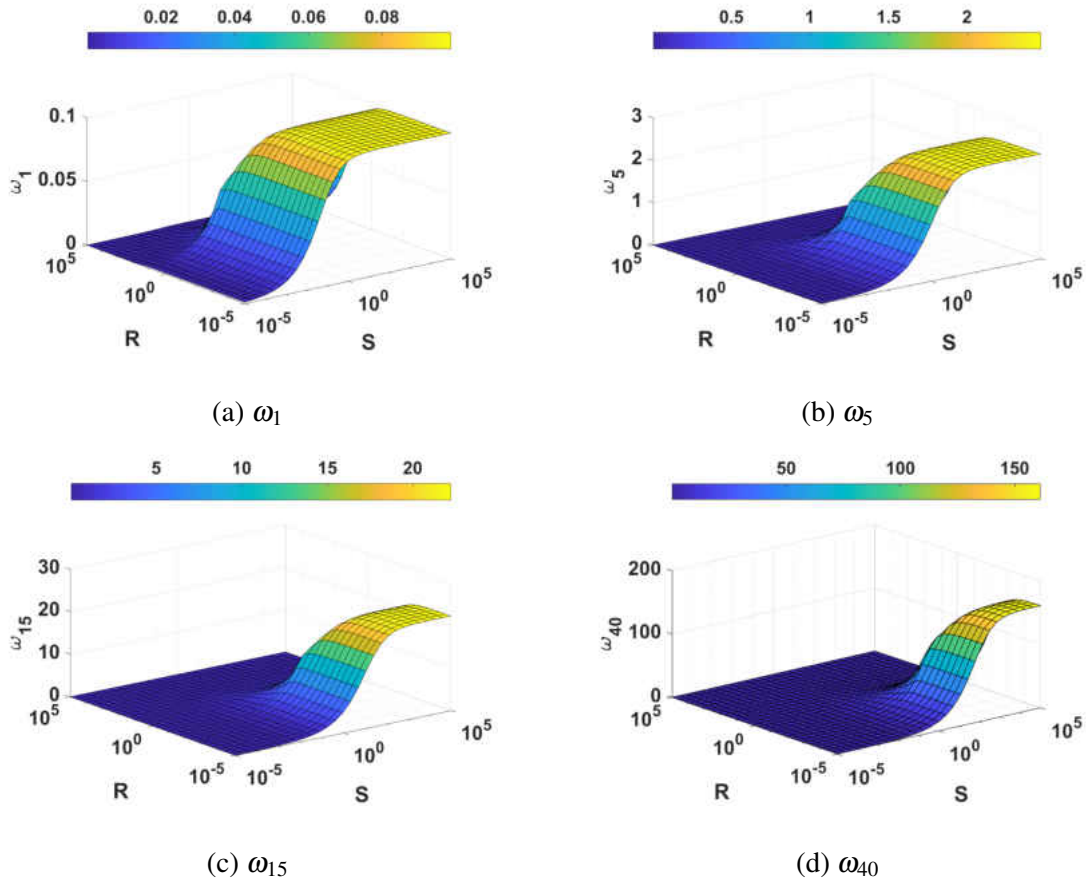


Figure 4.3: Surface plots of 1st, 5th, 15th and 40th mode natural frequencies with varying R and S values. Euler-Bernoulli, Timoshenko, Rayleigh, and shear beams are represented by the four corners.

Figure 4.4 shows a two-dimensional view of Figures 4.3a and 4.3d. Because previous models failed to accurately predict effects in the mid- to high-range frequencies, the R and S values used for this analysis are taken from the 40th mode frequency plot, as seen in Figure 4.4b. As mode number increases from Figure 4.4a to Figure 4.4b, the Euler-Bernoulli range decreases, and a wider range of R and S values can be used as Timoshenko beam properties.

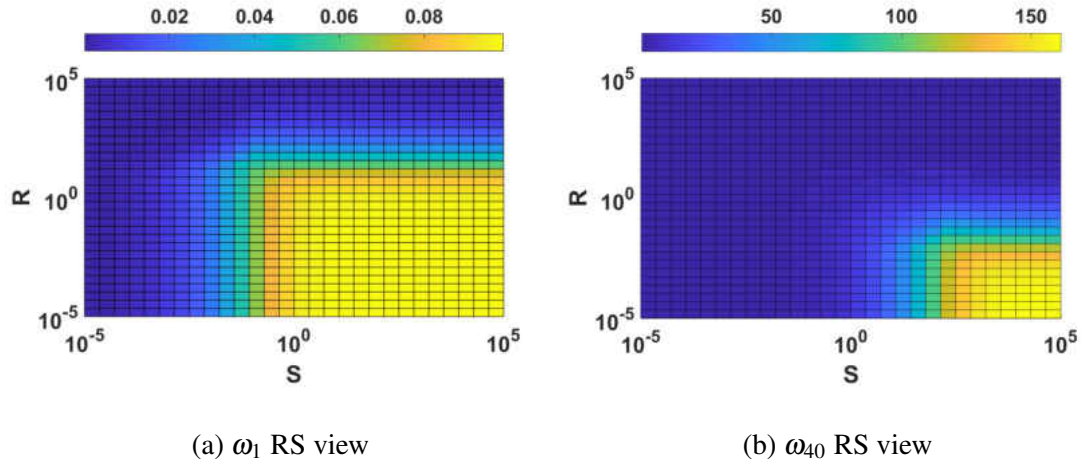


Figure 4.4: 2D view of 1st and 40th mode natural frequencies. As mode number increases, the Euler-Bernoulli range decreases and a larger number of R and S values indicate Timoshenko beams.

4.4 Damping Plots

Different combinations of damping terms in conjunction with varying weighting coefficients are used to investigate damping in Timoshenko beams as well as the possibility of producing approximately frequency-independent damping. Table 4.2 displays four combinations of R and S values selected from the 40th mode frequency plot. A visible representation of these cases is displayed in Figure 4.5. Euler-Bernoulli and Timoshenko cases are represented on opposite ends; as R increases and S decreases, values become closer to the Timoshenko range.

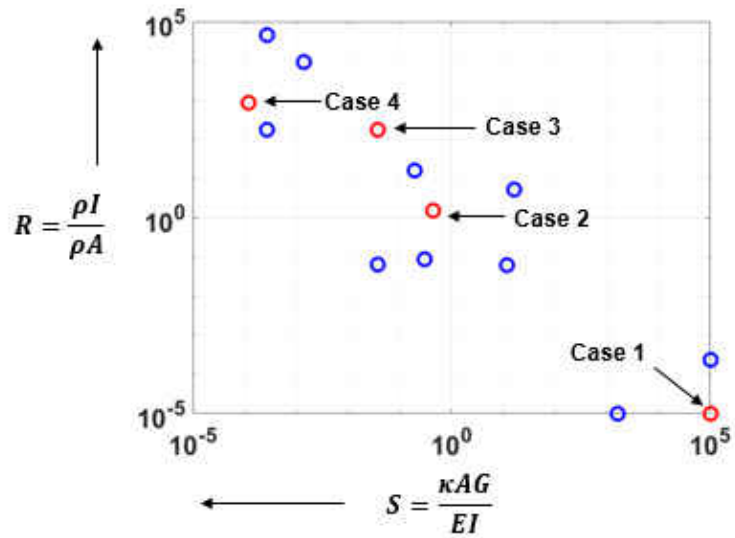


Figure 4.5: R and S values selected for the damping case study. As R increases and S decreases, values become further away from the Euler-Bernoulli case and extend into the Timoshenko region.

Table 4.2: R and S values used in the damping case study. Case 1 represents an Euler-Bernoulli model. Cases 2-4 are increasingly more in the Timoshenko region. Note the dimensions are given in meters, represented by m .

Case	1	2	3	4
R, m^2	1E-5	1.48	174.3	853.2
S, m^{-2}	1E5	.439	.03728	.1179E-3

Damping terms were previously divided into rotation-, motion-, and strain-based categories in Table 4.1. Beginning with the original ten damping terms created, the normalized damping ratios are plotted versus mode number for case 1. For this analysis, only the first 25 modes are studied.

The normalized damping values for an Euler-Bernoulli beam ($R = 1E-5 m^2$, $S = 1E5 m^{-2}$) are used to categorize the damping terms as motion-, strain-, or rotation-based damping.

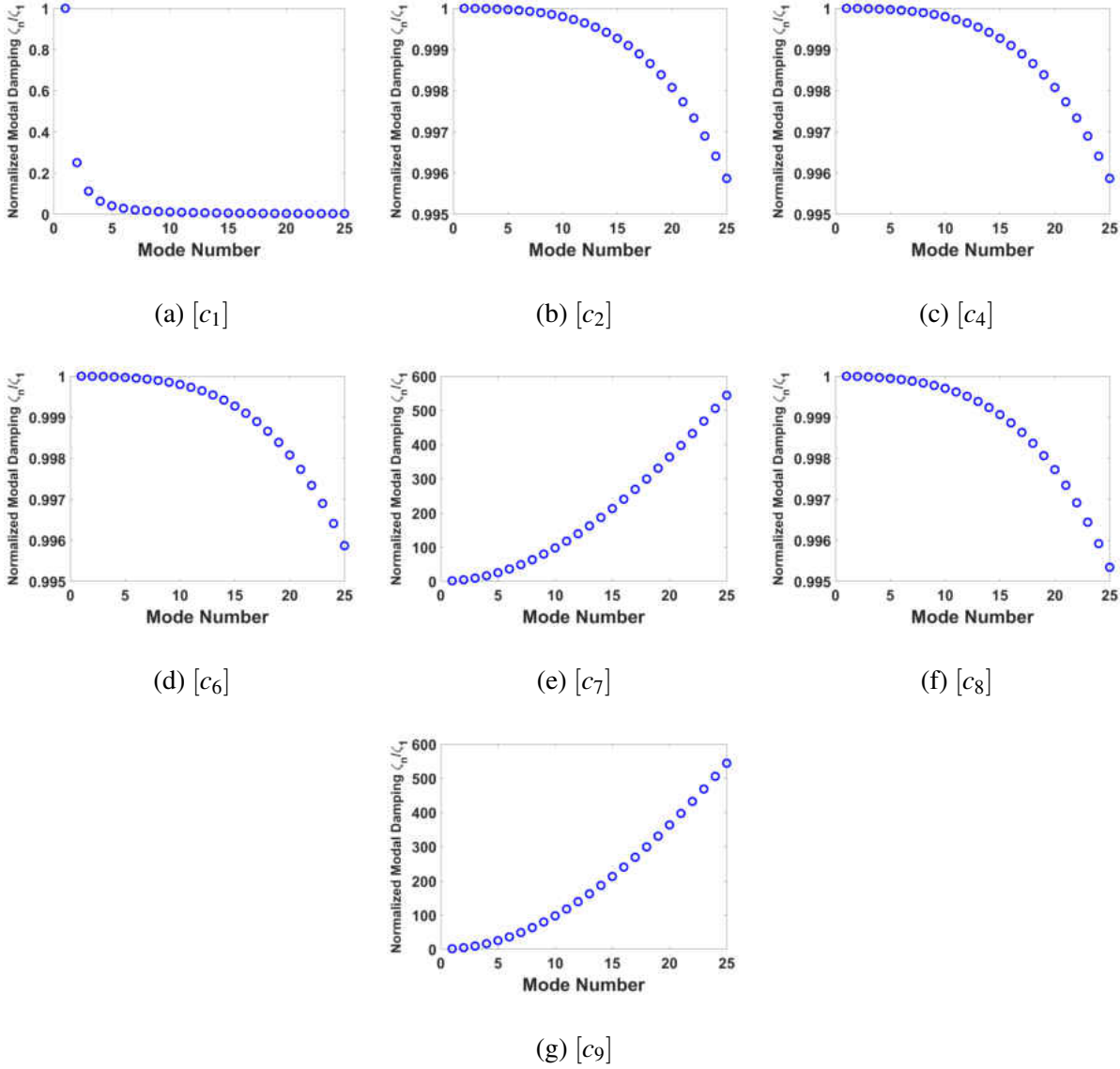
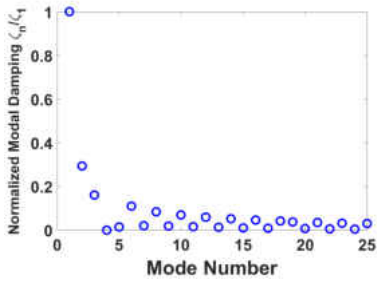
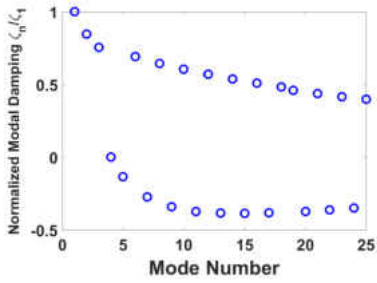


Figure 4.6: Case 1 (EB beam) damping ratios ($R = 1E-5 m^2$, $S = 1E5 m^{-2}$). Motion- ($1/m^2$), strain- ($1/m$), and rotation-based (≈ 1) damping terms are categorized from the damping ratio trends, where m is mode number.

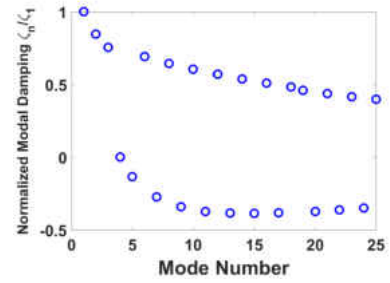
Figure 4.6 shows damping trends for R and S values representing an Euler-Bernoulli model; this region is defined by a very high shear value and very low rotary inertia parameter. Note that the scales on the y-axis vary between plots. Figure 4.6a displays normalized modal damping for $[c_1]$; the damping values are approximately proportional to $1/m^2$, where m is the mode number. This trend is typical in motion-based damping terms. Figures 4.6e and 4.6g show damping trends proportional to m^2 , typical of strain-based damping. Figures 4.6b to 4.6d and 4.6f display damping ratios that are approximately frequency-independent; these terms have been categorized as rotation-based damping terms. Again note the absence of $[c_3]$, $[c_5]$, and $[c_{10}]$; these terms produced zero damping and are not considered for the remaining cases.



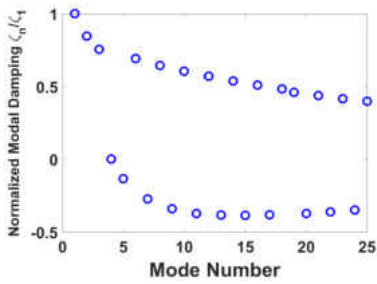
(a) $[c_1]$



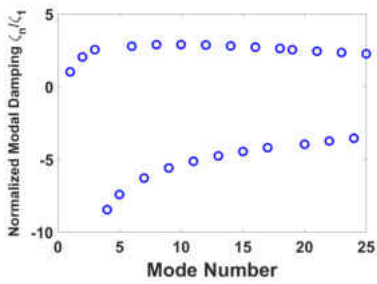
(b) $[c_2]$



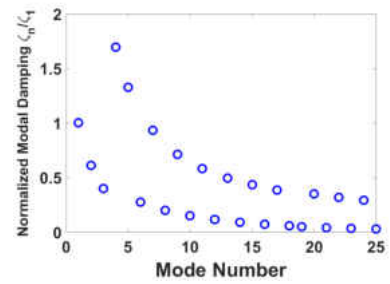
(c) $[c_4]$



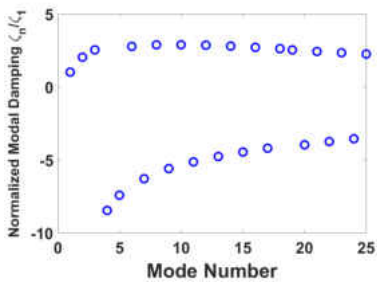
(d) $[c_6]$



(e) $[c_7]$

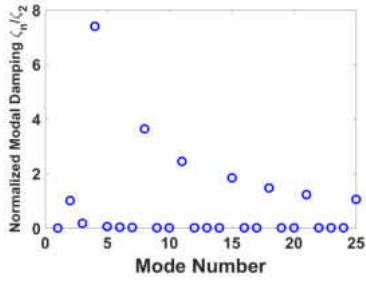


(f) $[c_8]$

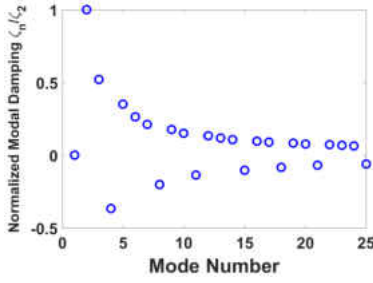


(g) $[c_9]$

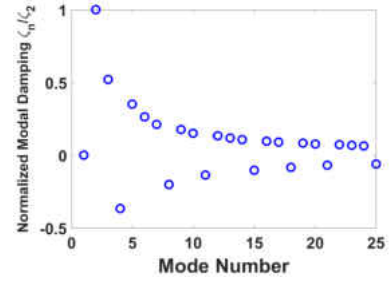
Figure 4.7: Case 2 damping ratios ($R = 1.48m^2$, $S = .439m^{-2}$). For Timoshenko regions, two damping trends emerge. Typical dependence ($1/m$, $1/m^2$) is no longer observed. Negative damping ratios also appear.



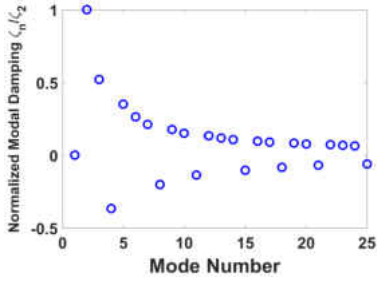
(a) $[c_1]$



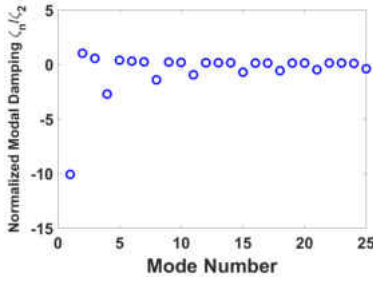
(b) $[c_2]$



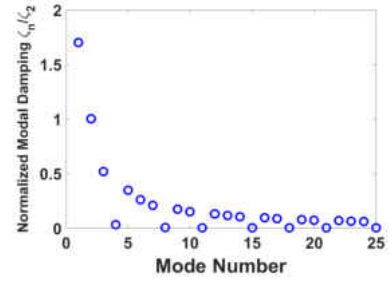
(c) $[c_4]$



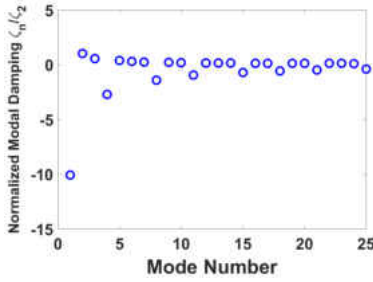
(d) $[c_6]$



(e) $[c_7]$

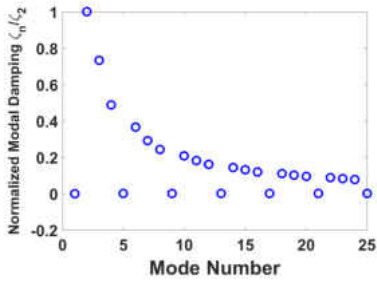


(f) $[c_8]$

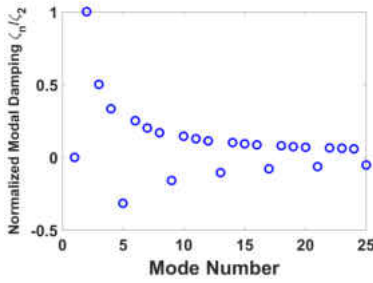


(g) $[c_9]$

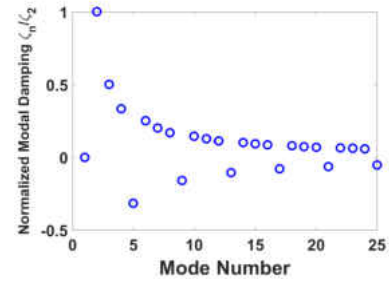
Figure 4.8: Case 3 damping ratios ($R = 174.3m^2$, $S = .03728m^{-2}$). As R and S values extend further into the Timoshenko region, larger variation in damping ratios occur. Negative damping still remains for 5 of the 7 damping terms.



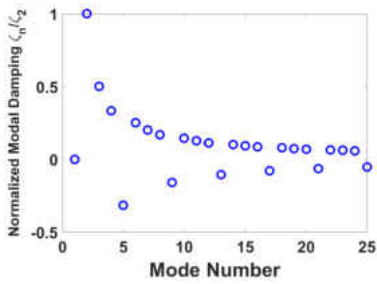
(a) $[c_1]$



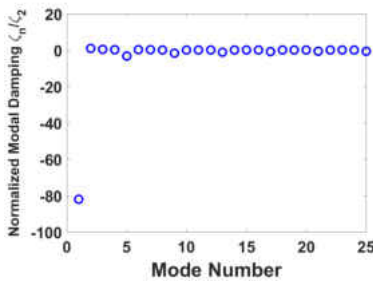
(b) $[c_2]$



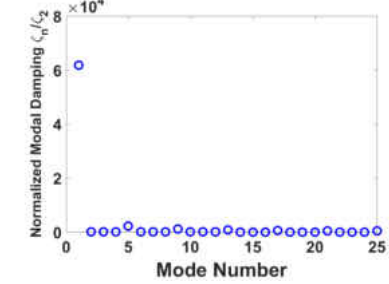
(c) $[c_4]$



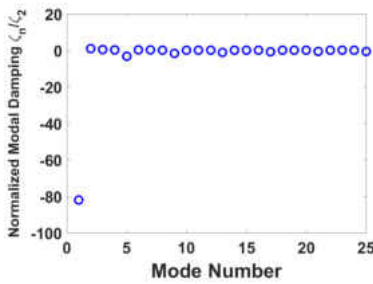
(d) $[c_6]$



(e) $[c_7]$



(f) $[c_8]$



(g) $[c_9]$

Figure 4.9: Case 4 damping ratios ($R = 856.2m^2$, $S = .1179E-3m^{-2}$). Damping ratios shown here have the highest shear and rotational effects. Three terms produce approximately zero damping for all modes, with 1 mode producing an extremely high damping value.

For the Timoshenko R and S values listed in Table 4.2, two separate trend lines appeared in the damping ratio plots (Figures 4.7 to 4.9). Previous work indicates a transition region between

bending-dominated and shear-dominated modes for shear beam formulations, where the damping ratios transition from m^2 to m proportional [11]. For the Timoshenko formulation, no clear transition region exists; instead the two trend lines developed indicated two sets of modes, dominated by shear, bending, or rotation. While two trends appear for all damping cases, the modes within each line differ on a case by case basis. Again note the changing scales of the y-axis. Cases 3 and 4 first mode damping are nominally zero, therefore these damping ratios are normalized by the second mode. Also note, in cases 1-3, a scaling factor $\alpha = .1$ was used; in case 4 $\alpha = .01$.

Damping terms initially categorized as rotation-based, $[c_2]$, $[c_4]$, $[c_6]$, and $[c_8]$, produced the same normalized damping for case 1. For cases 2-4, $[c_2]$, $[c_4]$, and $[c_6]$ produce identical results, but $[c_8]$ shows a unique trend. In the Euler-Bernoulli formulation, these terms produced frequency-independent damping; for the Timoshenko regions, one trend emerges that is similar to $1/m$ while another trend produces negative or approximately zero damping. Strain-based terms, $[c_7]$ and $[c_9]$, produced identical results for each case. While the results did not match typical strain-based damping (m), these terms exhibited less frequency-dependence in higher modes. The motion-based term $[c_1]$ produced a unique damping result, not matching any of the other terms. As the R and S values approach the “extreme” Timoshenko cases, more damping terms equaling approximately zero arise. Terms which produce negative damping are also of significant importance and could be used in future analysis to cancel out the effects of modes with extremely high damping ratios.

Other combinations of damping matrices are considered in addition to the original seven defined above. For example, in proportional damping, the damping matrix is defined as a combination of the stiffness and mass matrices using the relation $[C] = \alpha[M] + \beta[K]$. In this analysis, the mass

and stiffness terms are considered separately. Terms $[c_{14}] = \rho AN_{w_0w_0}$ and $[c_{15}] = \rho ARN_{t_0t_0}$ are the individual mass matrix components; $[c_{mmat}] = m_{mat}$ is the combined mass matrix. The stiffness matrix damping effects are examined as well, $[c_{kmat}] = k_{mat}$. Individual stiffness components, $[c_{12}] = N_{w_1w_1}$ and $[c_{16}] = N_{t_1t_1}$ were considered to further investigate the effects of transverse displacement and slope derivatives. As mentioned in a previous chapter, a symmetric damping matrix is of interest; using a damping term of the form $[c_{11}] = .5 * (N_{w_1t_0} + N_{t_0w_1})$ achieves a symmetric matrix. Combinations of terms, such as $[c_{13}] = [c_{11}] + [c_{12}]$ and $[c_{tot}] = [c_1] + [c_2] + \dots + [c_9]$ were used to investigate the possibility of frequency-independent damping. In addition, the total of all motion-, rotation-, and strain-based terms were examined, $[c_{mot}] = [c_1]$, $[c_{str}] = [c_7] + [c_9]$, $[c_{rot}] = [c_2] + [c_4] + [c_6] + [c_8]$. Figure 4.10 displays the above damping trends.

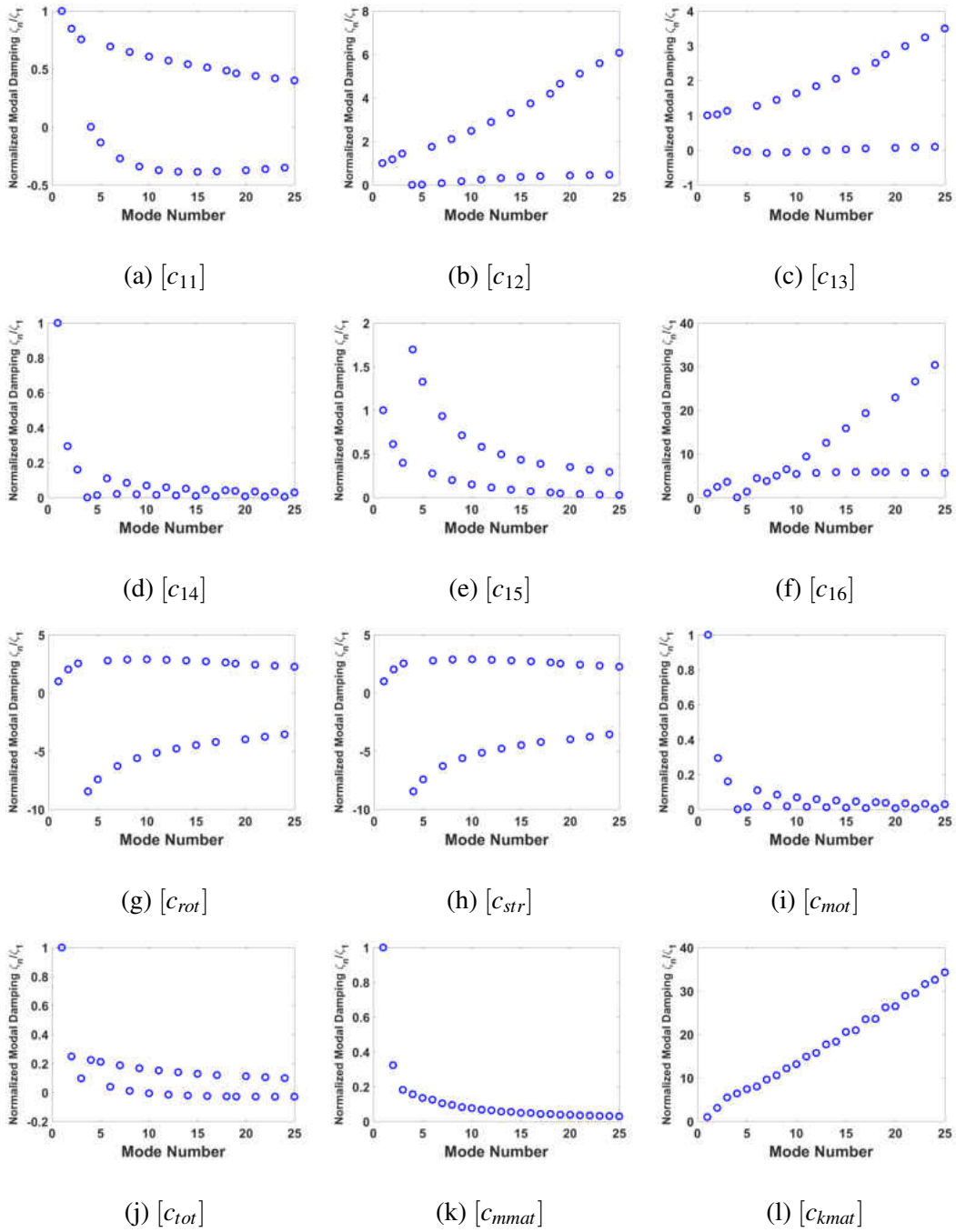
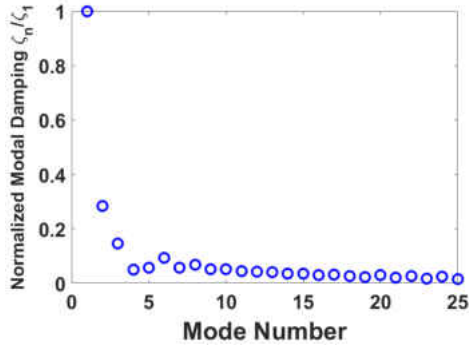


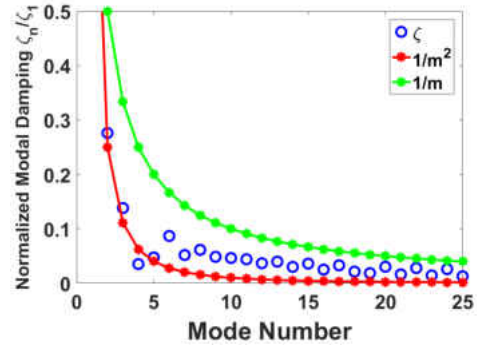
Figure 4.10: Additional damping terms are tested for case 2 values ($R = 1.48 m^2$, $S = .439 m^{-2}$). Components of proportional damping as well as combinations of a motion-, strain-, and rotation-based damping terms are displayed.

It is of interest to note that when the rotation- and strain-based damping terms are summed together (Figures 4.10g and 4.10h), the same results are produced. The motion-based and mass proportional damping terms produce ratios approximately proportional to $1/m^2$; strain-based and stiffness proportional terms produced linear trends. A typical proportional damping term ($[C] = \alpha[M] + \beta[K]$) could be created from summing together $[c_{kmat}]$ and $[c_{mmat}]$ and empirically fitting α and β coefficients. Terms $[c_{11}]$, $[c_{13}]$, $[c_{rot}]$, $[c_{str}]$, and $[c_{tot}]$ produced negative damping in certain modes; in order to use these in a valid model, these terms should be further investigated. Negative damping terms could be removed through a weighting factor, or with combinations of terms which cancel out negative trends.

While none of the above terms produced frequency-independent damping on their own, certain combinations were used to produce some frequency-independence; however, lower modes still displayed higher damping ratios, again demonstrating the unpredictability of Timoshenko damping. Figure 4.11a displays a combination of damping terms that reduced multiple trend lines to one as well as removed any negative damping terms. This particular combination includes damping coefficients in terms of R and S . Figure 4.11b shows a closer view of the damping ratios, revealing the results are between $1/m$ and $1/m^2$.



(a) Combination of damping terms $[c] = (1 + R/S)[c_1] + 2[c_4] + 2R[c_7] + [c_{11}]$.



(b) Zooming in on the y-axis reveals damping ratios between $1/m$ and $1/m^2$.

Figure 4.11: Combination of damping terms to investigate frequency-independent damping. A closer look reveals damping ratios between $1/m$ and $1/m^2$.

4.5 Beam Deformation

To better visualize the effects of R and S on damping, the beam deformations were plotted, including the effects of shear deformation, defined as $\beta = w' - \varphi$. Comparing the resulting deformation shapes to the trends observed in the damping ratio plots provides insight into the effect of bending-, shear-, or rotation-dominated regimes on each vibration mode. Previous work has indicated that motion- and strain-based damping terms in shear beam models transition from bending-dominated motion to shear-dominated motion; at this transition region, damping terms change their frequency-dependence, with damping ratios moving from m^2 to m proportional. Rotation-based damping terms were shown to experience a similar transition region; however, depending on the damping coefficient selected, rotation-based terms often displayed a steeper slope in the shear-dominated

regime. As Timoshenko damping displays, there is not a distinct point that can be viewed as a transition between bending- and shear-dominated regimes. Instead, it appears that two distinct trend lines occur across a wide range of modes, each within a certain motion type. Figure 4.12 displays $[c_{11}]$ damping values for case 2 R and S values. Trend 1 contains 14 modes, while trend 2 contains 11 modes.

Using a red-blue color map, shear deformation is indicated on the beam by the colored vertical lines. Red indicates a positive shear deformation, while blue indicates negative. As values fade to white, shear becomes smaller and reaches zero; darker shades of red and blue represent a larger shear deformation, while lighter shades represent smaller values. Rotational effects are indicated by the angle of the vertical lines, or the displacement of the “X” coordinate; a line perpendicular to the beam centerline, 90° , represents zero rotational effects. Bending is determined by the displacement of the top and bottom nodes, or the “Y” coordinate.

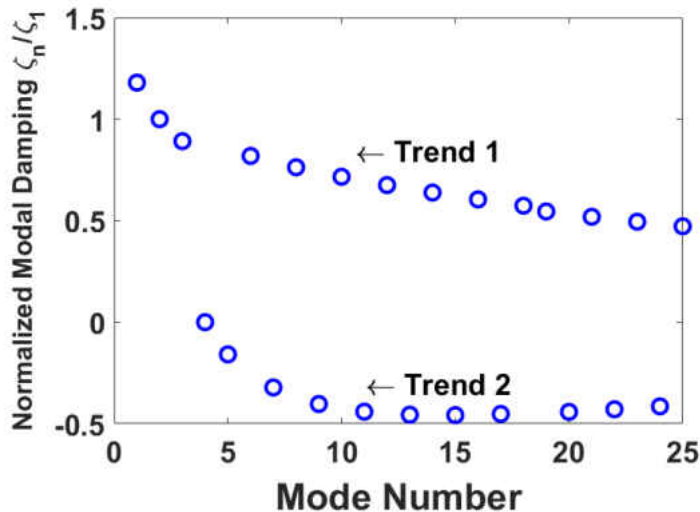
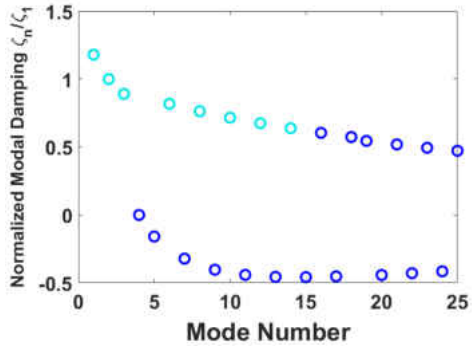
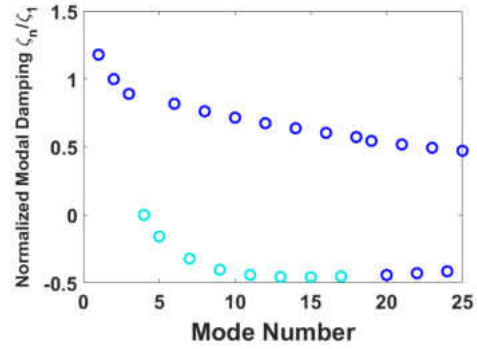


Figure 4.12: Case 2 $[c_{11}]$ damping. Two trend lines are identified in most Timoshenko damping plots. These trends correspond to deformed beam shapes.



(a) First 8 modes of trend 1 are shown in light blue. These modes correspond to bending-dominated regimes.



(b) First 8 modes of trend 2 are shown in light blue. These modes correspond to shear-dominated regimes.

Figure 4.13: Modes in light blue indicate those in the beam deformation plots. Both trend 1 and trend 2 modes were studied.

In Case 2, two damping trends emerge across all damping terms; the first is associated with modes 1, 2, 3, 6, 8, 10, 12, 14, 16, 18, 19, 21, 23, 25 and the second with modes 4, 5, 7, 9, 11, 13, 15, 17, 20, 22, 24. When investigating the deformed beam shapes, the exact same trends appeared in the beam deformation. Modes in trend 1 followed a typical pattern associated with beam bending. The first eight beam shapes in trend 1 are displayed in Figure 4.14 and are indicated by light blue circles in Figure 4.13a. Trend 2 modes exhibit more rotation- and shear-dominated motion, shown in Figure 4.15. The first 8 modes of trend 2 are displayed in Figure 4.13b. Only case 2 R and S values are shown, but case 3 and 4 trends also correlated to deformation type trends; however, the mode numbers in trends 1 and 2 differ between each case.

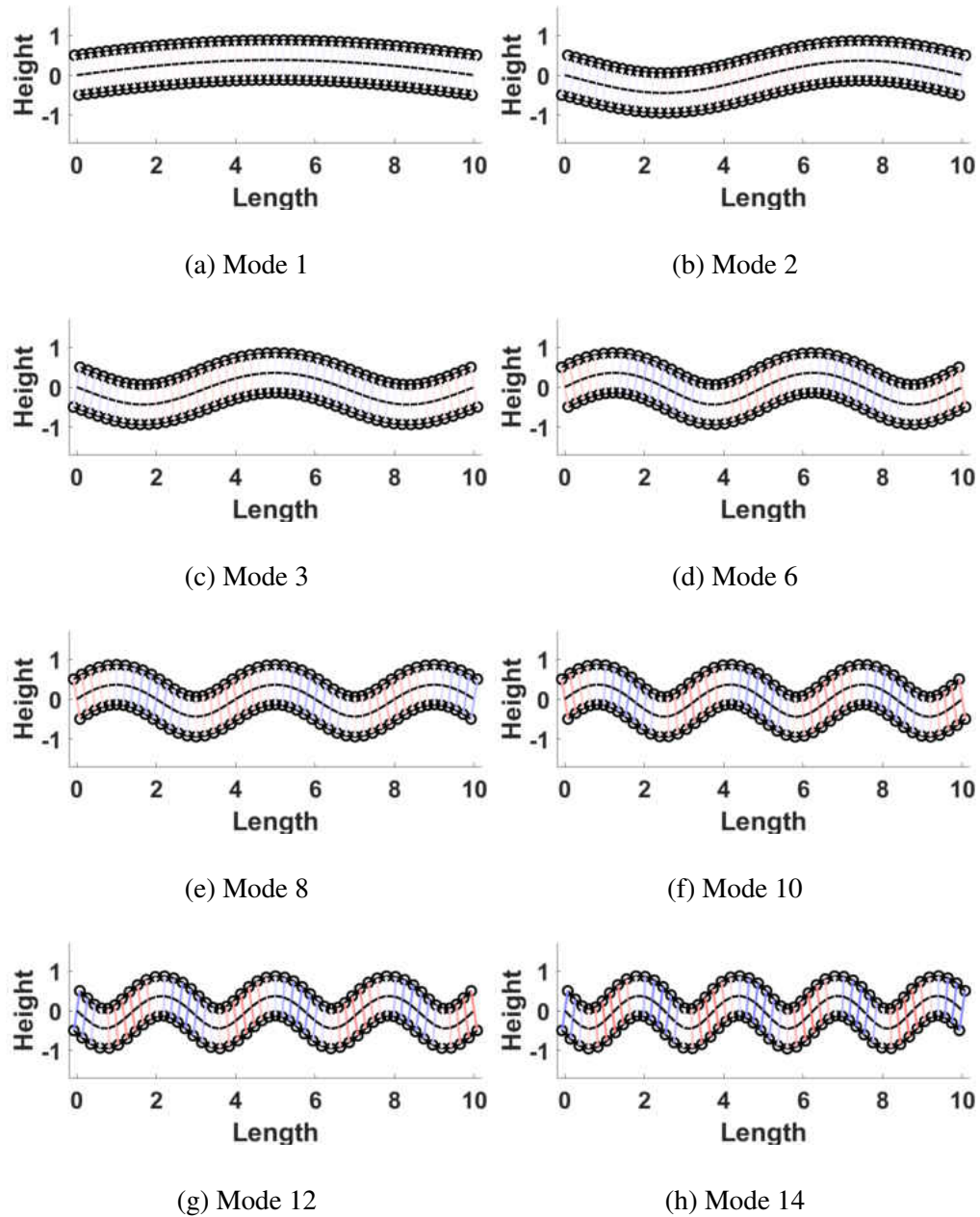


Figure 4.14: Modes 1, 2, 3, 6, 8, 10, 12, and 14 are the first 8 modes of trend 1. These modes display more dependence on bending-based deformation. These modes display very weak dependence on shear and rotation.

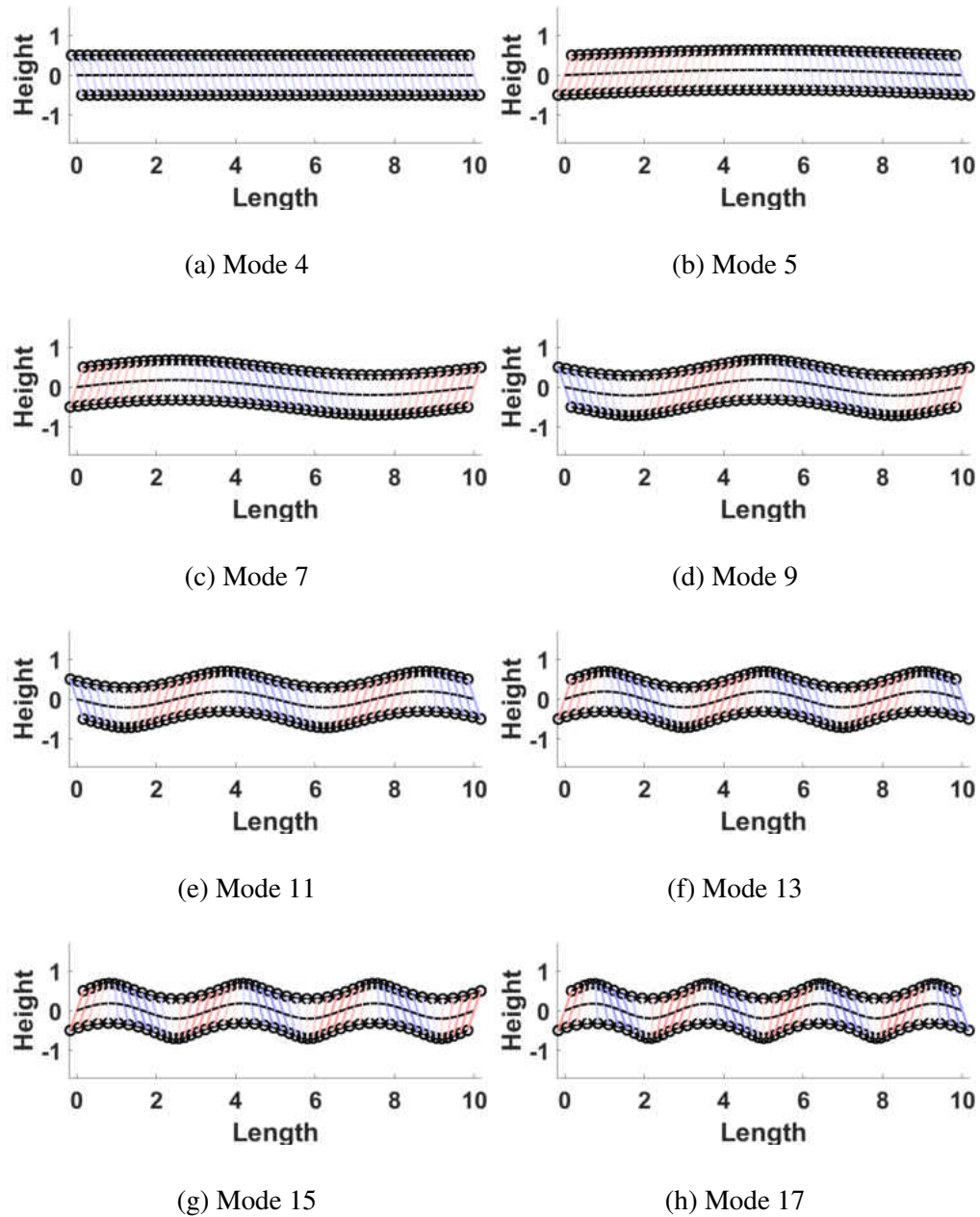


Figure 4.15: Modes 4, 5, 7, 9, 11, 13, 15, and 17 are the first 8 modes of trend 2. These modes display more dependence on shear- and rotation-based deformation. As mode number increases, both red and blue shades are darker, indicating an increase in shear.

CHAPTER 5

CONCLUSION

The primary goal of this work was to characterize damping in the Timoshenko range; knowledge gained from investigating the behavior of individual damping terms provides insight into the development of a frequency-independent damping model. Initially, method of weighted residuals was applied to the Timoshenko beam equations of motion to develop a finite element formulation. Two parameters R and S were used to quantify rotational inertia and transverse shear effects. Ten damping terms were created using third- and fourth-order spatial derivatives of the shape functions; only 7 of these terms produced non-zero damping.

5.1 Damping Results

Using rotational and shear parameters unique to an Euler-Bernoulli beam formulation (high S , low R), the ten initial damping terms were classified as motion-, strain-, or rotation-based damping based on the Euler-Bernoulli damping results. Of these terms, three produced no damping and were disregarded for the remainder of the analysis. Motion-based terms produced modal damping that was proportional to the inverse square of the mode number; shear-based damping was proportional

to the mode number squared. Rotation-based damping terms produced approximately frequency-independent damping.

When tested with parameters in the Timoshenko region (low S , high R), the damping terms produced results far different from those in the Euler-Bernoulli range, as expected. While Euler-Bernoulli beams produced a predictable, smooth trend line, the Timoshenko region produced highly unpredictable damping results. Two separate trend lines emerged for most damping terms; some modes produced significant damping, while others produced damping that was relatively small. When compared with the deformed beam shapes, similar trends occurred at the same modes. One trend was associated with bending deformation while another was related to shear, indicating the dominant type of deformation associated with a particular mode governed its associated modal damping value.

In addition to the ten damping terms in the equations of motion, various other terms were investigated; these terms included mass and stiffness proportional damping, a forced symmetric damping matrix, and various combinations of the damping terms in the equations of motion. Along with changing the scaling factors, these results aided in the investigation of frequency-independent damping across a large range of modes. An original hypothesis suggested that by scaling down specific damping terms and combining with others, damping trends merge into one approximately frequency-independent trend. With certain combinations, the first few modes almost always produced higher damping values and proved difficult to cancel out; however, the remaining modes exhibited greater frequency-independence.

5.2 Future Work

This work investigated damping in Timoshenko beams with a simply-supported connection. Future work will incorporate the same damping model with different boundary conditions. Previous work has modeled cables with free-free boundary conditions making it of higher interest in future analysis. Different boundary conditions may require a new combination of terms or a scaling factor unique to the connections tested to produce similar damping results. Different boundary conditions may also result in different Timoshenko trends not seen with the simply-supported case.

In addition, the negative damping terms produced by certain matrices warrant further investigation. These negative terms may be due to the combinations of damping types, as well as the complex nature of the Timoshenko range. For these negative terms to be used within a damping code, matrices producing negative damping ratios should be paired with terms that can cancel out these effects.

It is also of interest to revisit the residual integration by parts terms produced by method of weighted residuals. For certain boundary conditions, such as fixed-fixed, these terms should equal zero. However, this might not apply to all boundary conditions. When calculating the residual terms, it is also important to determine whether they should be applied to each local damping matrix, or only to the global matrix.

Beam deformation produced trends identical to the damping ratio trends. For the 3 cases provided, only the first 25 modes were investigated. Each case produced a varying amount of bending- or shear- and rotation-based modes. Future work will expand beyond mode 25; the patterns of de-

formation types for each case as well as the number of occurrences of each deformation type per case will be investigated. In addition, the first shear mode for multiple cases of R and S values will be recorded. By investigating the first appearance of a shear- or rotation-dominated mode, Timoshenko damping can be further characterized.

APPENDIX A
MATLAB CODE FOR BEAM NATURAL FREQUENCIES FEM

```

% TIMOSHENKO BEAM FINITE ELEMENT MODEL — FREQUENCY ANALYSIS
% Plots 3D surface plots of natural frequencies for varying R and S values
clc; clear all; close all;

% Some default commands for standardized graphics
set(0, 'DefaultAxesFontSize', 24, 'DefaultTextFontSize', 24, ...
    'DefaultAxesFontName', 'Helvetica', ...
    'DefaultTextFontName', 'Helvetica', ...
    'DefaultAxesFontWeight', 'bold', 'DefaultTextFontWeight', 'bold', ...
    'DefaultLineLineWidth', 3, 'DefaultLineMarkerSize', 12, ...
    'DefaultFigureColor', 'w', 'DefaultAxesColorOrder', ...
    [0 0 1; 0 .5 0; 1 0 0; 0 .75 .75; .75 0 .75; .75 .75 0; .25 .25 .25], ...
    'DefaultFigurePosition', [5 100 [900 650]*.9], ...
    'DefaultFigureResize', 'off')

format shorte
%% Set up for variable number of elements
Nel = 50; % Number of elements
L = 10; % Beam length
rhoA = 1; % Beam density (per length)
EI = 1; % Beam flexural rigidity
R = logspace(-5, 5, 30); % Inertia parameter (= I/A)
S = logspace(-5, 5, 30); % Shear parameter (= kAG/EI)

%% TIMOSHENKO
% Begin FE setup — element length, phi parameter, and local matrices
% built from shape functions
%     nw0w0 is integral_0^Lel [N_w]^T [N_w] dx
%     ntlw1 is integral_0^Lel [N_phi']^T [N_w'] dx
%     etc.
Lel = L/Nel;
for j = 1:length(R)
    for k = 1:length(S)
        phi = 12/S(k)/Lel^2; %Timoshenko

        nw0w0 = 1/840/(1+phi)^2*Lel*...
            [4*(78+147*phi+70*phi^2) Lel*(44+77*phi+35*phi^2) ...
            4*(27+63*phi+35*phi^2) -Lel*(26+63*phi+35*phi^2);
            Lel*(44+77*phi+35*phi^2) Lel^2*(8+14*phi+7*phi^2) ...
            Lel*(26+63*phi+35*phi^2) -Lel^2*(6+14*phi+7*phi^2);
            4*(27+63*phi+35*phi^2) Lel*(26+63*phi+35*phi^2) ...
            4*(78+147*phi+70*phi^2) -Lel*(44+77*phi+35*phi^2);
            -Lel*(26+63*phi+35*phi^2) -Lel^2*(6+14*phi+7*phi^2) ...
            -Lel*(44+77*phi+35*phi^2) Lel^2*(8+14*phi+7*phi^2)];

        ntlw1 = 1/60/(1+phi)^2/Lel*...
            [12*(6+10*phi+5*phi^2) 6*Lel ...
            -12*(6+10*phi+5*phi^2) 6*Lel;
            6*Lel Lel^2*(8+10*phi+5*phi^2) ...
            -6*Lel -Lel^2*(2+10*phi+5*phi^2)];
    end
end

```

```

-12*(6+10*phi+5*phi^2)      -6*Lel ...
12*(6+10*phi+5*phi^2)      -6*Lel;
6*Lel                       -Lel^2*(2+10*phi+5*phi^2) ...
-6*Lel                       Lel^2*(8+10*phi+5*phi^2)];

nt0t0 = 1/30/(1+phi)^2/Lel*...
[36                          -3*Lel*(-1+5*phi) ...
-36                          -3*Lel*(-1+5*phi);
-3*Lel*(-1+5*phi)          Lel^2*(4+5*phi+10*phi^2) ...
3*Lel*(-1+5*phi)          Lel^2*(-1-5*phi+5*phi^2);
-36                        3*Lel*(-1+5*phi) ...
36                          3*Lel*(-1+5*phi);
-3*Lel*(-1+5*phi)          Lel^2*(-1-5*phi+5*phi^2) ...
3*Lel*(-1+5*phi)          Lel^2*(4+5*phi+10*phi^2)];

nt1t1 = 1/(1+phi)^2/Lel^3*...
[12      6*Lel              -12      6*Lel;
6*Lel  Lel^2*(4+2*phi+phi^2) -6*Lel -Lel^2*(-2+2*phi+phi^2);
-12    -6*Lel              12      -6*Lel;
6*Lel  -Lel^2*(-2+2*phi+phi^2) -6*Lel  Lel^2*(4+2*phi+phi^2)];

nw0t1 = 1/60/(1+phi)^2/Lel*...
[-72-60*phi                -6*Lel*(11+15*phi+5*phi^2) ...
72+60*phi                  6*Lel*(-1+5*phi+5*phi^2);
-6*Lel                     -Lel^2*(8+10*phi+5*phi^2) ...
6*Lel                      Lel^2*(2+10*phi+5*phi^2);
72+60*phi                  -6*Lel*(-1+5*phi+5*phi^2) ...
-72-60*phi                 6*Lel*(11+15*phi+5*phi^2);
-6*Lel                     Lel^2*(2+10*phi+5*phi^2) ...
6*Lel                      -Lel^2*(8+10*phi+5*phi^2)];

nt1w0 = nw0t1';

nw1t0 = 1/60/(1+phi)^2/Lel*...
[72+60*phi                -6*Lel*(-1+5*phi+5*phi^2) ...
-72-60*phi                -6*Lel*(-1+5*phi+5*phi^2);
6*Lel                     Lel^2*(8+10*phi+5*phi^2) ...
-6*Lel                    -Lel^2*(2+10*phi+5*phi^2);
-72-60*phi                6*Lel*(-1+5*phi+5*phi^2) ...
72+60*phi                 6*Lel*(-1+5*phi+5*phi^2);
6*Lel                     -Lel^2*(2+10*phi+5*phi^2) ...
-6*Lel                    Lel^2*(8+10*phi+5*phi^2)];

nt0w1 = nw1t0';

% Initialize mass, stiffness, & damping matrices; calculate in \
%terms of shape function matrices above

%Variable R/S values
mmat = zeros(4,4); kmat = mmat;
mmat = nw0w0 + R(j)*nt0t0;
kmatt = nt1t1 + S(k)*nw1w1 + S(k)*nt0t0 - S(k)*nw1t0 - S(k)*nt0w1;

```



```

% Initialize & construct global mass, stiffness, and damping
% matrices
K = zeros(2*Nel+2);
M = K;

for n=1:Nel
    i1 = 2*n-1; i2 = 2*n+2;
    K(i1:i2,i1:i2) = K(i1:i2,i1:i2) + EI*kmat;
    M(i1:i2,i1:i2) = M(i1:i2,i1:i2) + rhoA*mmat;
end

% Apply boundary conditions (un-comment the one of interest and
% comment out the rest)

% Pinned-Pinned
K(1,:) = []; K(:,1) = []; K(end-1,:) = []; K(:,end-1) = [];
M(1,:) = []; M(:,1) = []; M(end-1,:) = []; M(:,end-1) = [];

% % Clamped-Clamped
% K(1:2,:) = []; K(:,1:2) = []; K(end-1:end,:) = [];
%K(:,end-1:end) = [];
% M(1:2,:) = []; M(:,1:2) = []; M(end-1:end,:) = [];
%M(:,end-1:end) = [];

% % Clamped-Free
% K(1:2,:) = []; K(:,1:2) = []; % M(1:2,:) = []; M(:,1:2) = [];

% % Clamped-Pinned
% K(1:2,:) = []; K(:,1:2) = []; K(end-1,:) = []; K(:,end-1) = [];
% M(1:2,:) = []; M(:,1:2) = []; M(end-1,:) = []; M(:,end-1) = [];

% Solve eigenvalue problem in first-order form; sort modes and
% compute natural frequencies and damping ratios

[v,d] = eig(K,M); % solve eigenvalue problem
[omgr,ind] = sort(sqrt(diag(d))); % find omega_n and sort modes
freqs(:,j,k) = omgr;

end
end
freqs1 = squeeze(freqs(1, :, :));
freqs5 = squeeze(freqs(5, :, :));
freqs15 = squeeze(freqs(15, :, :));
freqs40 = squeeze(freqs(40, :, :));

figure; surf(S,R,freqs1);
xlabel('S'); ylabel('R'); zlabel('\omega_{1}')
set(gca, 'XScale', 'log', 'YScale', 'log');
shading faceted; colorbar('northoutside');

figure; surf(S,R,freqs5);

```

```
xlabel('S'); ylabel('R'); zlabel('\omega_{5}')
set(gca, 'XScale', 'log', 'YScale', 'log');
shading faceted; colorbar('northoutside')

figure; surf(S,R,freqs15);
xlabel('S'); ylabel('R'); zlabel('\omega_{15}')
set(gca, 'XScale', 'log', 'YScale', 'log');
shading faceted; colorbar('northoutside')

figure; hold on; surf(R,S,freqs40); grid on
xlabel('S'); ylabel('R'); zlabel('\omega_{40}')
set(gca, 'XScale', 'log', 'YScale', 'log');
shading faceted; colorbar('northoutside')
```

APPENDIX B
MATLAB CODE FOR BEAM DAMPING FEM

```

% TIMOSHENKO BEAM FINITE ELEMENT MODEL
% Written by Jeffrey L. Kauffman & Brandi McPherson

clc; clear all; close all;

% Some default commands for standardized graphics
set(0,'DefaultAxesFontSize',24,'DefaultTextFontSize',24,...
    'DefaultAxesFontName','Helvetica',...
    'DefaultTextFontName','Helvetica',...
    'DefaultAxesFontWeight','bold','DefaultTextFontWeight','bold',...
    'DefaultLineLineWidth',3,'DefaultLineMarkerSize',12,...
    'DefaultFigureColor','w','DefaultAxesColorOrder',...
    [0 0 1;0 .5 0;1 0 0;0 .75 .75;.75 0 .75;.75 .75 0;.25 .25 .25],...
    'DefaultFigurePosition',[5 100 [900 650]*.9],...
    'DefaultFigureResize','off')

format short
%% Set up for variable number of elements
Nel = 50; % Number of elements
L = 10; % Beam length
rhoA = 1; % Beam density (per length)
EI = 1; % Beam flexural rigidity
R = 1.48; % R = rhoI/rhoA
S = .439; % S = kAG/EI
%%%%%%%%%%%%%%%%%%%%%%%%%%%%%%%%%%%%%%%%%%%%%%%%%%%%%%%%%%%%%%%%%%%%%%%%

for ie = 1:length(Nel)
    % Begin FE setup — element length, phi parameter, and local matrices
    % built from shape functions
    %     nw0w0 is integral_0^Lel [N_w]^T [N_w] dx
    %     ntlw1 is integral_0^Lel [N_phi']^T [N_w] dx
    %     etc.
    Lel = L/Nel(ie);
    phi = 12/S/Lel^2; %Timoshenko

    nw0w0 = 1/840/(1+phi)^2*Lel*...
        [4*(78+147*phi+70*phi^2) Lel*(44+77*phi+35*phi^2) ...
        4*(27+63*phi+35*phi^2) -Lel*(26+63*phi+35*phi^2);
        Lel*(44+77*phi+35*phi^2) Lel^2*(8+14*phi+7*phi^2) ...
        Lel*(26+63*phi+35*phi^2) -Lel^2*(6+14*phi+7*phi^2);
        4*(27+63*phi+35*phi^2) Lel*(26+63*phi+35*phi^2) ...
        4*(78+147*phi+70*phi^2) -Lel*(44+77*phi+35*phi^2);
        -Lel*(26+63*phi+35*phi^2) -Lel^2*(6+14*phi+7*phi^2) ...
        -Lel*(44+77*phi+35*phi^2) Lel^2*(8+14*phi+7*phi^2)];

    ntlw1 = 1/60/(1+phi)^2/Lel*...
        [12*(6+10*phi+5*phi^2) 6*Lel ...
        -12*(6+10*phi+5*phi^2) 6*Lel;
        6*Lel Lel^2*(8+10*phi+5*phi^2) ...
        -6*Lel -Lel^2*(2+10*phi+5*phi^2);
        -12*(6+10*phi+5*phi^2) -6*Lel ...

```

```

12*(6+10*phi+5*phi^2)      -6*Lel;
6*Lel                       -Lel^2*(2+10*phi+5*phi^2) ...
-6*Lel                       Lel^2*(8+10*phi+5*phi^2)];

nt0t0 = 1/30/(1+phi)^2/Lel*...
[36                          -3*Lel*(-1+5*phi) ...
-36                          -3*Lel*(-1+5*phi);
-3*Lel*(-1+5*phi)           Lel^2*(4+5*phi+10*phi^2) ...
3*Lel*(-1+5*phi)           Lel^2*(-1-5*phi+5*phi^2);
-36                          3*Lel*(-1+5*phi) ...
36                           3*Lel*(-1+5*phi);
-3*Lel*(-1+5*phi)           Lel^2*(-1-5*phi+5*phi^2) ...
3*Lel*(-1+5*phi)           Lel^2*(4+5*phi+10*phi^2)];

nt1t1 = 1/(1+phi)^2/Lel^3*...
[12      6*Lel      -12      6*Lel      ;
6*Lel  Lel^2*(4+2*phi+phi^2) -6*Lel  -Lel^2*(-2+2*phi+phi^2);
-12    -6*Lel      12     -6*Lel      ;
6*Lel  -Lel^2*(-2+2*phi+phi^2) -6*Lel  Lel^2*(4+2*phi+phi^2)  ];

nw0t1 = 1/60/(1+phi)^2/Lel*...
[-72-60*phi      -6*Lel*(11+15*phi+5*phi^2) ...
72+60*phi         6*Lel*(-1+5*phi+5*phi^2);
-6*Lel            -Lel^2*(8+10*phi+5*phi^2) ...
6*Lel            Lel^2*(2+10*phi+5*phi^2);
72+60*phi        -6*Lel*(-1+5*phi+5*phi^2) ...
-72-60*phi       6*Lel*(11+15*phi+5*phi^2);
-6*Lel           Lel^2*(2+10*phi+5*phi^2) ...
6*Lel           -Lel^2*(8+10*phi+5*phi^2)];

nt1w0 = nw0t1';

nw1t0 = 1/60/(1+phi)^2/Lel*...
[72+60*phi      -6*Lel*(-1+5*phi+5*phi^2) ...
-72-60*phi      -6*Lel*(-1+5*phi+5*phi^2);
6*Lel           Lel^2*(8+10*phi+5*phi^2) ...
-6*Lel          -Lel^2*(2+10*phi+5*phi^2);
-72-60*phi      6*Lel*(-1+5*phi+5*phi^2) ...
72+60*phi       6*Lel*(-1+5*phi+5*phi^2);
6*Lel           -Lel^2*(2+10*phi+5*phi^2) ...
-6*Lel          Lel^2*(8+10*phi+5*phi^2)];

nt0w1 = nw1t0';

nw0w2 = [ -(phi + 6/5)/(Lel*(phi + 1)^2), ...
- (phi/2 + 3/5)/(phi + 1)^2 - 1/2, ...
(phi + 6/5)/(Lel*(phi + 1)^2), 1/2 - (phi/2 + 3/5)/(phi + 1)^2;
-1/(10*(phi + 1)^2), ...
- Lel/12 - Lel/(20*(phi + 1)^2), ...
1/(10*(phi + 1)^2), Lel/12 - Lel/(20*(phi + 1)^2);
(phi + 6/5)/(Lel*(phi + 1)^2), ...

```

```

(phi/2 + 3/5)/(phi + 1)^2 - 1/2, ...
-(phi + 6/5)/(Lel*(phi + 1)^2), (phi/2 + 3/5)/(phi + 1)^2 + 1/2;
-1/(10*(phi + 1)^2), Lel/12 - Lel/(20*(phi + 1)^2), ...
1/(10*(phi + 1)^2), - Lel/12 - Lel/(20*(phi + 1)^2)];

nw0w4 = [ 0, 0, 0, 0;
          0, 0, 0, 0;
          0, 0, 0, 0;
          0, 0, 0, 0];

nt0w3 = [-12/(Lel^3*(phi + 1)^2),    -6/(Lel^2*(phi + 1)^2),    ...
          12/(Lel^3*(phi + 1)^2),    -6/(Lel^2*(phi + 1)^2);
          (6*phi)/(Lel^2*(phi + 1)^2), (3*phi)/(Lel*(phi + 1)^2), ...
          -(6*phi)/(Lel^2*(phi + 1)^2), (3*phi)/(Lel*(phi + 1)^2);
          12/(Lel^3*(phi + 1)^2),    6/(Lel^2*(phi + 1)^2),    ...
          -12/(Lel^3*(phi + 1)^2),    6/(Lel^2*(phi + 1)^2);
          (6*phi)/(Lel^2*(phi + 1)^2), (3*phi)/(Lel*(phi + 1)^2), ...
          -(6*phi)/(Lel^2*(phi + 1)^2), (3*phi)/(Lel*(phi + 1)^2)];

nw0t3 = [ 0, 0, 0, 0;
          0, 0, 0, 0;
          0, 0, 0, 0;
          0, 0, 0, 0];

nt0t2 = [ -12/(Lel^3*(phi + 1)^2),    -6/(Lel^2*(phi + 1)^2), ...
          12/(Lel^3*(phi + 1)^2),    -6/(Lel^2*(phi + 1)^2);
          (6*phi)/(Lel^2*(phi + 1)^2), (3*phi)/(Lel*(phi + 1)^2), ...
          -(6*phi)/(Lel^2*(phi + 1)^2), (3*phi)/(Lel*(phi + 1)^2);
          12/(Lel^3*(phi + 1)^2),    6/(Lel^2*(phi + 1)^2),    ...
          -12/(Lel^3*(phi + 1)^2),    6/(Lel^2*(phi + 1)^2);
          (6*phi)/(Lel^2*(phi + 1)^2), (3*phi)/(Lel*(phi + 1)^2), ...
          -(6*phi)/(Lel^2*(phi + 1)^2), (3*phi)/(Lel*(phi + 1)^2)];

nt0t3 = [ 0, 0, 0, 0;
          0, 0, 0, 0;
          0, 0, 0, 0;
          0, 0, 0, 0];

nw2w2 = [ 12/(Lel^3*(phi + 1)^2),    6/(Lel^2*(phi + 1)^2), ...
          -12/(Lel^3*(phi + 1)^2),    6/(Lel^2*(phi + 1)^2);
          6/(Lel^2*(phi + 1)^2), 3/(Lel*(phi + 1)^2) + 1/Lel, ...
          -6/(Lel^2*(phi + 1)^2), 3/(Lel*(phi + 1)^2) - 1/Lel;
          -12/(Lel^3*(phi + 1)^2),    -6/(Lel^2*(phi + 1)^2), ...
          12/(Lel^3*(phi + 1)^2),    -6/(Lel^2*(phi + 1)^2);
          6/(Lel^2*(phi + 1)^2), 3/(Lel*(phi + 1)^2) - 1/Lel, ...

```

```

-6/(Lel^2*(phi + 1)^2), 3/(Lel*(phi + 1)^2) + 1/Lel];

nt2t2 = [ 144/(Lel^5*(phi + 1)^2), 72/(Lel^4*(phi + 1)^2), ...
-144/(Lel^5*(phi + 1)^2), 72/(Lel^4*(phi + 1)^2);
72/(Lel^4*(phi + 1)^2), 36/(Lel^3*(phi + 1)^2), ...
-72/(Lel^4*(phi + 1)^2), 36/(Lel^3*(phi + 1)^2);
-144/(Lel^5*(phi + 1)^2), -72/(Lel^4*(phi + 1)^2), ...
144/(Lel^5*(phi + 1)^2), -72/(Lel^4*(phi + 1)^2);
72/(Lel^4*(phi + 1)^2), 36/(Lel^3*(phi + 1)^2), ...
-72/(Lel^4*(phi + 1)^2), 36/(Lel^3*(phi + 1)^2)];

ntlw2 = [ 12/(Lel^3*(phi + 1)^2), 6/(Lel^2*(phi + 1)^2), ...
-12/(Lel^3*(phi + 1)^2), 6/(Lel^2*(phi + 1)^2);
6/(Lel^2*(phi + 1)^2), 3/(Lel*(phi + 1)^2) + 1/Lel, ...
-6/(Lel^2*(phi + 1)^2), 3/(Lel*(phi + 1)^2) - 1/Lel;
-12/(Lel^3*(phi + 1)^2), -6/(Lel^2*(phi + 1)^2), ...
12/(Lel^3*(phi + 1)^2), -6/(Lel^2*(phi + 1)^2);
6/(Lel^2*(phi + 1)^2), 3/(Lel*(phi + 1)^2) - 1/Lel, ...
-6/(Lel^2*(phi + 1)^2), 3/(Lel*(phi + 1)^2) + 1/Lel];

nw1t2 = [ -12/(Lel^3*(phi + 1)), -6/(Lel^2*(phi + 1)), ...
12/(Lel^3*(phi + 1)), -6/(Lel^2*(phi + 1));
0, 0, ...
0, 0;
12/(Lel^3*(phi + 1)), 6/(Lel^2*(phi + 1)), ...
-12/(Lel^3*(phi + 1)), 6/(Lel^2*(phi + 1));
0, 0, ...
0, 0];

nt0t4 = [ 0, 0, 0, 0;
0, 0, 0, 0;
0, 0, 0, 0;
0, 0, 0, 0];

nw0w1 = [- 3*phi - 3, (Lel*(5*phi + 6))/10, 3*phi + 3, ...
-(Lel*(5*phi + 6))/10;
-(Lel*(5*phi + 6))/10, 0, (Lel*(5*phi + 6))/10, -Lel^2/10;
- 3*phi - 3, -(Lel*(5*phi + 6))/10, 3*phi + 3, ...
(Lel*(5*phi + 6))/10;
(Lel*(5*phi + 6))/10, Lel^2/10, -(Lel*(5*phi + 6))/10, 0];

nw0w3 = [ 6/(Lel^2*(phi + 1)), 3/(Lel*(phi + 1)), ...
-6/(Lel^2*(phi + 1)), 3/(Lel*(phi + 1));
1/(Lel*(phi + 1)), 1/(2*(phi + 1)), ...
-1/(Lel*(phi + 1)), 1/(2*(phi + 1));
6/(Lel^2*(phi + 1)), 3/(Lel*(phi + 1)), ...
-6/(Lel^2*(phi + 1)), 3/(Lel*(phi + 1));
-1/(Lel*(phi + 1)), -1/(2*(phi + 1)), ...

```

```

1/(Lel*(phi + 1)), -1/(2*(phi + 1))];

nt0t1 = [ 0, 1/(Lel*(phi + 1)), 0, -1/(Lel*(phi + 1));
-1/(Lel*(phi + 1)), -1/2, 1/(Lel*(phi + 1)), 1/2 - 1/(phi + 1);
0, -1/(Lel*(phi + 1)), 0, 1/(Lel*(phi + 1));
1/(Lel*(phi + 1)), 1/(phi + 1) - 1/2, -1/(Lel*(phi + 1)), 1/2];

% Initialize mass, stiffness, & damping matrices; calculate in terms of
% shape function matrices above
mmat = zeros(4,4); kmat = mmat;
mmat = nw0w0 + R*nt0t0;
mrhoI = R*nt0t0; mrhoA = nw0w0;
kmat = nt1t1 + S*nw1w1 + S*nt0t0 -S*nw1t0 - S*nt0w1;
cmat1 = nw0w0;
cmat2 = nw0w2;
cmat3 = nw0w4;
cmat4 = nw0t1;
cmat5 = nw0t3;
cmat6 = nt0w1;
cmat7 = nt0w3;
cmat8 = nt0t0;
cmat9 = nt0t2;
cmat10 = nt0t4;
cmat11 = .5*(nw1t0 + nt0w1);
cmat12 = nw1w1;
cmat13 = cmat11 + cmat12;
cmat14 = rhoA*nw0w0;
cmat15 = rhoA*R*nt0t0;
cmat16 = nt1t1;
crot = cmat2 + cmat4 + cmat6 + cmat8;
cmot = cmat1;
cstr = cmat7 + cmat9;
ctot = cmat1+cmat2+cmat3+cmat4+cmat5+cmat6+cmat7+cmat8+cmat9+cmat10;
cind1 = cmat1*(1+R/S) + 2*cmat4 + 2*R*cmat7 + cmat11
cind2 = cmat1*(1+R/S) + 2*cmat4 + 2*R*cmat7 + S*cmat11

% Initialize & construct global mass, stiffness, and damping matrices
K = zeros(2*Nel(ie)+2); Cind = zeros(2*Nel(ie)+2,2*Nel(ie)+2,25);
M = K; MrhoA = K; MrhoI = K;

for n=1:Nel(ie)
    i1 = 2*n-1; i2 = 2*n+2;
    %Stiffness Matrix
    K(i1:i2,i1:i2) = K(i1:i2,i1:i2) + EI*kmat;
    %Effect of individual damping terms
    Cind(i1:i2,i1:i2,1) = Cind(i1:i2,i1:i2,1) + cmat1;
    Cind(i1:i2,i1:i2,2) = Cind(i1:i2,i1:i2,2) + cmat2;
    Cind(i1:i2,i1:i2,3) = Cind(i1:i2,i1:i2,3) + cmat3; %0
    Cind(i1:i2,i1:i2,4) = Cind(i1:i2,i1:i2,4) + cmat4;
    Cind(i1:i2,i1:i2,5) = Cind(i1:i2,i1:i2,5) + cmat5; %0
    Cind(i1:i2,i1:i2,6) = Cind(i1:i2,i1:i2,6) + cmat6;

```



```

Cind(i1:i2,i1:i2,7) = Cind(i1:i2,i1:i2,7) + cmat7;
Cind(i1:i2,i1:i2,8) = Cind(i1:i2,i1:i2,8) + cmat8;
Cind(i1:i2,i1:i2,9) = Cind(i1:i2,i1:i2,9) + cmat9;
Cind(i1:i2,i1:i2,10) = Cind(i1:i2,i1:i2,10) + cmat10; %0
Cind(i1:i2,i1:i2,11) = Cind(i1:i2,i1:i2,11) + cmat11;
Cind(i1:i2,i1:i2,12) = Cind(i1:i2,i1:i2,12) + cmat12;
Cind(i1:i2,i1:i2,13) = Cind(i1:i2,i1:i2,13) + cmat13;
Cind(i1:i2,i1:i2,14) = Cind(i1:i2,i1:i2,14) + cmat14;
Cind(i1:i2,i1:i2,15) = Cind(i1:i2,i1:i2,15) + cmat15;
%Using stiffness and mass as damping
Cind(i1:i2,i1:i2,16) = Cind(i1:i2,i1:i2,16) + crot;
Cind(i1:i2,i1:i2,17) = Cind(i1:i2,i1:i2,17) + cstr;
Cind(i1:i2,i1:i2,18) = Cind(i1:i2,i1:i2,18) + cmot;
Cind(i1:i2,i1:i2,19) = Cind(i1:i2,i1:i2,19) + ctot;
Cind(i1:i2,i1:i2,20) = Cind(i1:i2,i1:i2,20) + cind1;
%Additional Damping Terms
Cind(i1:i2,i1:i2,21) = Cind(i1:i2,i1:i2,21) + rhoA*mmat;
Cind(i1:i2,i1:i2,22) = Cind(i1:i2,i1:i2,22) + kmat;
Cind(i1:i2,i1:i2,23) = Cind(i1:i2,i1:i2,23) + cmat16;
Cind(i1:i2,i1:i2,24) = Cind(i1:i2,i1:i2,24) + cind2;
Cind(i1:i2,i1:i2,25) = Cind(i1:i2,i1:i2,25) + S*kmat+ rhoA*mmat;
%Mass Matrix
M(i1:i2,i1:i2) = M(i1:i2,i1:i2) + rhoA*mmat;
MrhoA(i1:i2,i1:i2) = MrhoA(i1:i2,i1:i2) + rhoA*mrhoA;
MrhoI(i1:i2,i1:i2) = MrhoI(i1:i2,i1:i2) + rhoA*mrhoI;
end

% Apply boundary conditions (un-comment the one of interest and comment
% out the rest)

% Pinned-Pinned
K(1,:) = []; K(:,1) = []; K(end-1,:) = []; K(:,end-1) = [];
Cind(1,,:) = []; Cind(:,1,:) = []; Cind(end-1,,:) = [];
Cind(:,end-1,:) = [];
M(1,:) = []; M(:,1) = []; M(end-1,:) = []; M(:,end-1) = [];

% % Clamped-Clamped
% K(1:2,:) = []; K(:,1:2) = []; K(end-1:end,:) = []; K(:,end-1:end)=[];
% C(1:2,:) = []; C(:,1:2) = []; C(end-1:end,:) = []; C(:,end-1:end)=[];
% M(1:2,:) = []; M(:,1:2) = []; M(end-1:end,:) = []; M(:,end-1:end)=[];

% % Clamped-Free
% K(1:2,:) = []; K(:,1:2) = [];
% C(1:2,:) = []; C(:,1:2) = [];
% M(1:2,:) = []; M(:,1:2) = [];

% % Clamped-Pinned
% K(1:2,:) = []; K(:,1:2) = []; K(end-1,:) = []; K(:,end-1) = [];
% C(1:2,:) = []; C(:,1:2) = []; C(end-1,:) = []; C(:,end-1) = [];
% M(1:2,:) = []; M(:,1:2) = []; M(end-1,:) = []; M(:,end-1) = [];

```

```

% Solve eigenvalue problem in first-order form; sort modes and compute
% natural frequencies and damping ratios

%To observe effects of individual damping terms...
for i = [1:10]
    clearvars damps freqs
    C(:, :, i) = Cind(:, :, i)*.01;
    val_damp = eig([C(:, :, i) K;-eye(size(K)) zeros(size(K))],...
        [M zeros(size(K));zeros(size(K)) eye(size(K))]);
    val_damp_sort = sort(val_damp);
    freqs = abs(val_damp_sort);
    damps = real(val_damp_sort)./abs(val_damp_sort);
    damps = damps(1:2:end)
    damps = damps/damps(1); %normalize

    %Plot modal damping ratios versus mode number
    figure(i);
    plot(damps(1:25), 'bo'); hold on;
    xl = xlabel('Mode Number');
    yl = ylabel('Normalized Modal Damping \zeta_n/\zeta_1');
    set(xl, 'fontsize', 30)
    set(yl, 'fontsize', 22)
end
end

```

APPENDIX C
MATLAB CODE FOR BEAM DEFORMATION

```

%% Timoshenko Beam Deformation
% updated: May 23, 2017

clc; clear all; close all;

% Some default commands for standardized graphics
set(0,'DefaultAxesFontSize',24,'DefaultTextFontSize',24,...
    'DefaultAxesFontName','Helvetica',...
    'DefaultTextFontName','Helvetica',...
    'DefaultAxesFontWeight','bold','DefaultTextFontWeight','bold',...
    'DefaultLineLineWidth',3,'DefaultLineMarkerSize',12,...
    'DefaultFigureColor','w','DefaultAxesColorOrder',...
    [0 0 1;0 .5 0;1 0 0;0 .75 .75;.75 0 .75;.75 .75 0;.25 .25 .25],...
    'DefaultFigurePosition',[5 100 [900 420]*.9],'DefaultFigureResize',...
    'off')

% User Inputs Below
Nel = 50; % Number of elements
L = 10; % Beam length
h = 1; % beam height
rhoA = 1; % Beam density (per length)
EI = 1 ; % Beam flexural rigidity
R = 174.3; % R = rhoI/rhoA
S = .03728; % S = kAG/EI

% Begin FE setup — element length, phi parameter, and local matrices
% built from shape functions
%     nw0w0 is integral_0^Lel [N_w]^T [N_w] dx
%     ntlw1 is integral_0^Lel [N_phi']^T [N_w'] dx
%     etc.
Lel = L/Nel;
phi = 12/S/Lel^2;

nw0w0 = 1/840/(1+phi)^2*Lel*...
    [4*(78+147*phi+70*phi^2) Lel*(44+77*phi+35*phi^2) ...
    4*(27+63*phi+35*phi^2) -Lel*(26+63*phi+35*phi^2);
    Lel*(44+77*phi+35*phi^2) Lel^2*(8+14*phi+7*phi^2) ...
    Lel*(26+63*phi+35*phi^2) -Lel^2*(6+14*phi+7*phi^2);
    4*(27+63*phi+35*phi^2) Lel*(26+63*phi+35*phi^2) ...
    4*(78+147*phi+70*phi^2) -Lel*(44+77*phi+35*phi^2);
    -Lel*(26+63*phi+35*phi^2) -Lel^2*(6+14*phi+7*phi^2) ...
    -Lel*(44+77*phi+35*phi^2) Lel^2*(8+14*phi+7*phi^2)];

ntlw1 = 1/60/(1+phi)^2/Lel*...
    [12*(6+10*phi+5*phi^2) 6*Lel ...
    -12*(6+10*phi+5*phi^2) 6*Lel;
    6*Lel Lel^2*(8+10*phi+5*phi^2) ...
    -6*Lel -Lel^2*(2+10*phi+5*phi^2);
    -12*(6+10*phi+5*phi^2) -6*Lel ...
    12*(6+10*phi+5*phi^2) -6*Lel];

```

```

6*Lel          -Lel^2*(2+10*phi+5*phi^2) ...
-6*Lel          Lel^2*(8+10*phi+5*phi^2)];

nt0t0 = 1/30/(1+phi)^2/Lel*...
[36          -3*Lel*(-1+5*phi) ...
-36          -3*Lel*(-1+5*phi);
-3*Lel*(-1+5*phi) Lel^2*(4+5*phi+10*phi^2) ...
3*Lel*(-1+5*phi) Lel^2*(-1-5*phi+5*phi^2);
-36          3*Lel*(-1+5*phi) ...
36          3*Lel*(-1+5*phi);
-3*Lel*(-1+5*phi) Lel^2*(-1-5*phi+5*phi^2) ...
3*Lel*(-1+5*phi) Lel^2*(4+5*phi+10*phi^2)];

nt1t1 = 1/(1+phi)^2/Lel^3*...
[12      6*Lel          -12      6*Lel          ;
6*Lel  Lel^2*(4+2*phi+phi^2) -6*Lel  -Lel^2*(-2+2*phi+phi^2);
-12    -6*Lel          12      -6*Lel          ;
6*Lel  -Lel^2*(-2+2*phi+phi^2) -6*Lel  Lel^2*(4+2*phi+phi^2)  ];

nw0t1 = 1/60/(1+phi)^2/Lel*...
[-72-60*phi          -6*Lel*(11+15*phi+5*phi^2) ...
72+60*phi          6*Lel*(-1+5*phi+5*phi^2);
-6*Lel          -Lel^2*(8+10*phi+5*phi^2) ...
6*Lel          Lel^2*(2+10*phi+5*phi^2);
72+60*phi          -6*Lel*(-1+5*phi+5*phi^2) ...
-72-60*phi          6*Lel*(11+15*phi+5*phi^2);
-6*Lel          Lel^2*(2+10*phi+5*phi^2) ...
6*Lel          -Lel^2*(8+10*phi+5*phi^2)];

nt1w0 = nw0t1';

nw1t0 = 1/60/(1+phi)^2/Lel*...
[72+60*phi          -6*Lel*(-1+5*phi+5*phi^2) ...
-72-60*phi          -6*Lel*(-1+5*phi+5*phi^2);
6*Lel          Lel^2*(8+10*phi+5*phi^2) ...
-6*Lel          -Lel^2*(2+10*phi+5*phi^2);
-72-60*phi          6*Lel*(-1+5*phi+5*phi^2) ...
72+60*phi          6*Lel*(-1+5*phi+5*phi^2);
6*Lel          -Lel^2*(2+10*phi+5*phi^2) ...
-6*Lel          Lel^2*(8+10*phi+5*phi^2)];

nt0w1 = 1/60/(1+phi)^2/Lel*...
[72+60*phi          6*Lel ...
-72-60*phi          6*Lel;
-6*Lel*(-1+5*phi+5*phi^2) Lel^2*(8+10*phi+5*phi^2) ...
6*Lel*(-1+5*phi+5*phi^2) -Lel^2*(2+10*phi+5*phi^2);
-72-60*phi          -6*Lel ...
72+60*phi          -6*Lel;
-6*Lel*(-1+5*phi+5*phi^2) -Lel^2*(2+10*phi+5*phi^2) ...
6*Lel*(-1+5*phi+5*phi^2) Lel^2*(8+10*phi+5*phi^2)];

```

```

% Initialize mass, stiffness, & damping matrices; calculate in terms of
% shape function matrices above
mmat = zeros(4,4); kmat = mmat;
mmat = nw0w0 + R*nt0t0;
kmat = ntl1t1 + S*nw1w1 + S*nt0t0 -S*nw1t0 - S*nt0w1;

% Initialize & construct global mass, stiffness, and damping matrices
K = zeros(2*Nel+2); C = K; M = K;

for n=1:Nel
    i1 = 2*n-1; i2 = 2*n+2;
    K(i1:i2,i1:i2) = K(i1:i2,i1:i2) + EI*kmats;
    M(i1:i2,i1:i2) = M(i1:i2,i1:i2) + rhoA*mmat;
end

% Apply boundary conditions (un-comment the one of interest and comment
% out the rest)

% Pinned-Pinned
K(1,:) = []; K(:,1) = []; K(end-1,:) = []; K(:,end-1) = [];

M(1,:) = []; M(:,1) = []; M(end-1,:) = []; M(:,end-1) = [];

% % Clamped-Clamped
% K(1:2,:) = []; K(:,1:2) = []; K(end-1:end,:) = []; K(:,end-1:end) = [];
% M(1:2,:) = []; M(:,1:2) = []; M(end-1:end,:) = []; M(:,end-1:end) = [];

% % Clamped-Free
% K(1:2,:) = []; K(:,1:2) = [];
% M(1:2,:) = []; M(:,1:2) = [];

% % Clamped-Pinned
% K(1:2,:) = []; K(:,1:2) = []; K(end-1,:) = []; K(:,end-1) = [];
% M(1:2,:) = []; M(:,1:2) = []; M(end-1,:) = []; M(:,end-1) = [];

% Solve eigenvalue problem in first-order form; sort modes and compute
% natural frequencies and damping ratios
Nc = size(K,1);
[v,d] = eig(K,M); % solve eigenvalue problem
[omgr,ind] = sort(sqrt(diag(d))); % find omega_n and sort modes

for r = 1:Nc % sorted & normalized using mass
    Phic(:,r) = v(:,ind(r))/sqrt(v(:,ind(r))'*M*v(:,ind(r)));
    % constrained e'vecs, column-wise
end

%Restore zeros
% Pinned-Pinned

```

```

Phi = [zeros(1,Nc); Phic(1:end-1,:); zeros(1,Nc); Phic(end,:)];

% Clamped-Clamped
% Phi = [zeros(2,Nc); Phic; zeros(2,Nc)];

% Clamped-Free
% Phi = [zeros(2,Nc); Phic];

% Clamped-Pinned
% Phi = [zeros(2,Nc); Phic(1:end-1,:); zeros(1,Nc); Phic(end,:)];

% plotting deformed beam
mode = [1:25];
Nw_p = [-(phi*Lel^2 + 6*Lel*0 - 6*0^2)/(Lel^3*(phi + 1)), ...
        (Lel*(phi/2 + 1)/Lel + (3*0^2)/Lel^3 - ...
        (2*0*(phi/2 + 2))/Lel^2)/(phi + 1), ...
        (phi*Lel^2 + 6*Lel*0 - 6*0^2)/(Lel^3*(phi + 1)), ...
        -(4*Lel*0 + Lel^2*phi - 6*0^2 - ...
        2*Lel*phi*0)/(2*Lel^2*(phi + 1))];
Nphi = [(6/(Lel*(1+phi)))*((0/Lel)^2 - (0/Lel)), ...
        (1/(1+phi))*(3*(0/Lel)^2-(4 + phi)*(0/Lel)+(1+phi)), ...
        -(6/(Lel*(1+phi)))*((0/Lel)^2-(0/Lel)), ...
        (1/(1+phi))*(3*(0/Lel)^2-(2-phi)*(0/Lel))];
xnode = linspace(0,L,Nel+1); % array of x at the nodes, or x original

%Shape function derivatives to solve for w'
for j = 1:length(xnode)-1
    w_p(j,:) = Nw_p*Phi((2*j-1):(2*j-1)+3,:);
    rot(j,:) = Nphi*Phi((2*j-1):(2*j-1)+3,:);
end
w_p(length(xnode),:) = [-(phi*Lel^2 + 6*Lel*Lel - ...
    6*Lel^2)/(Lel^3*(phi + 1)), ...
    (Lel*((phi/2 + 1)/Lel + (3*Lel^2)/Lel^3 - ...
    (2*Lel*(phi/2 + 2))/Lel^2))/(phi + 1), ...
    (phi*Lel^2 + 6*Lel*Lel - 6*Lel^2)/(Lel^3*(phi + 1)), ...
    -(4*Lel*Lel + Lel^2*phi - 6*Lel^2 - ...
    2*Lel*phi*Lel)/(2*Lel^2*(phi + 1))*Phi((end-3:end),:);
rot(length(xnode),:) = [(6/(Lel*(1+phi)))*((Lel/Lel)^2 - (Lel/Lel)), ...
    (1/(1+phi))*(3*(Lel/Lel)^2-(4 + phi)*(Lel/Lel)+(1+phi)), ...
    -(6/(Lel*(1+phi)))*((Lel/Lel)^2-(Lel/Lel)), ...
    (1/(1+phi))*(3*(Lel/Lel)^2-(2-phi)*(Lel/Lel))]*Phi((end-3:end),:);
beta = w_p - rot;

N_colorstep = 50;
color_scale = redbluemap(N_colorstep);

for count = 1:length(mode)
    for i = 1:count
        beta = beta(:,mode); %to use for max beta in modes in mode vector
        beta_scale(i) = max(abs(beta(:)))*1.000001;
    end
end

```

```

    %scaled by max beta at all modes
    for n = 1:length(xnode)
        colorbin(n,i) = round((N.colorstep/2/beta_scale(i))*...
            (beta(n,i) + (N.colorstep/2+.5)));
    end
end

for i = 1:length(count)
    zdef = Phi(1:2:end,count(i))-h/2*(1-cos(Phi(1:2:end,count(i))));
    xdef = h/2*sin(Phi(2:2:end,count(i)));

    %plot deformed
    figure(count); hold on;
    plot(xnode - xdef', h/2 + zdef, '-ok', ...
        xnode + xdef', -h/2 + zdef, '-ok')

    %plot vertical lines
    for j = 1:length(xnode)
        hold on; axis equal;
        x = [xnode(j) - xdef(j), xnode(j) + xdef(j)'];
        y = [h/2 + zdef(j), -h/2 + zdef(j)];
        plot(x,y, 'color', color_scale(colorbin(j,count), :));

        %plot centerline
        if j < length(xnode)
            x = [xnode(j), xnode(j+1)];
            y = [zdef(j), zdef(j+1)];
            plot(x,y, 'k—');
        else
            end
    end

end

end

axis([0-.2 L+.2 -1-.7 1+.7]);
xlabel('Length'); ylabel('Height')
set(gca, 'FontSize', 30);
set(gca, 'LooseInset', get(gca, 'TightInset'))
end

```


LIST OF REFERENCES

- [1] Kauffman JL, Lesieutre GA (2013) “Damping models for timoshenko beams with applications to spacecraft wiring harnesses,” *54th AIAA/ASME/ASCE/AHS/ASC Structures, Structural Dynamics, and Materials Conference*, page 1890. doi:10.2514/6.2013-1890
- [2] Ardelean EV, Babuska V, Goodding JC, Coombs DM, Robertson LM, Lane SA (2015) “Cable effects study: Tangents, rabbit holes, dead ends, and valuable results,” *Journal of Spacecraft and Rockets* 52 (2): 569–583. doi:10.2514/1.A32792
- [3] Goodding JC, Ardelean EV, Babuska V, Robertson LM, Lane SA (2011) “Experimental techniques and structural parameter estimation studies of spacecraft cables,” *Journal of Spacecraft and Rockets* 48 (6): 942–957. doi:10.2514/1.49346
- [4] Babuska V, Coombs DM, Goodding JC, Ardelean EV, Robertson LM, Lane SA (2010) “Modeling and experimental validation of space structures with wiring harnesses,” *Journal of Spacecraft and Rockets* 47 (6): 1038–1052. doi:10.2514/1.48078
- [5] Lesieutre GA (2010) “Frequency-independent modal damping for flexural structures via a viscous ”geometric” damping model,” *Journal of Guidance, Control, and Dynamics* 33 (6): 1931–1935. doi:10.2514/1.49864
- [6] Kauffman JL, Lesieutre GA (2013) “Geometric viscous damping model for nearly constant beam modal damping,” *AIAA Journal* 51 (7): 1688–1964. doi:10.2514/1.J052174
- [7] Johnson CD, Kienholz DA (1981) “Finite element prediction of damping in structures with constrained viscoelastic layers,” *22nd Structures, Structural Dynamics and Materials Conference*,. doi:10.2514/6.1981-486
- [8] Soroka WW (2012) “Note on the relations between viscous and structural damping coefficients,” *Journal of the Aeronautical Sciences* 16 (7): 409–410. doi:10.2514/8.11822
- [9] Coombs DM, Goodding JC, Babuska V, Ardelean EV, Roberston LM, Lane SA (2011) “Dynamic Modeling and Experimental Validation of a Cable-Loaded Panel,” *Journal of Spacecraft and Rockets* 48 (6): 958–973. doi:10.2514/1.51021
- [10] Lundén R, Åkesson B (1983) “Damped second-order rayleigh-timoshenko beam vibration in spacean exact complex dynamic member stiffness matrix,” *International Journal for Numerical Methods in Engineering* 19 (3): 431–449. doi:10.1002/nme.1620190310

- [11] Kauffman JL, Lesieutre GA, Babuska V (2014) “Damping models for shear beams with applications to spacecraft wiring harnesses,” *Journal of Spacecraft Rockets* 51 (1): 16–22. doi:10.2514/1.A32440
- [12] Ardelean E, Goodding J, Mehle G, Coombs D, Babuska V, Robertson L, Lane S, Ingram B, Hansen E (2007) “Dynamics of cable harnesses on large precision structures,” *48th AIAA/ASME/ASCE/AHS/ASC Structures, Structural Dynamics, and Materials Conference*, page 2388. doi:10.2514/6.2007-2388
- [13] NASA. *Crimping, Interconnecting Cables, Harnesses, and Wiring*, February 1998.
- [14] Society of Automotive Engineers. *Wiring, Aerospace Vehicles*, September 1998.
- [15] ESA. *Guidelines for Spacecraft Power and Signal Cabling*, February 1978.
- [16] Goodding JC (2008) “Spacecraft electrical cable harness structural test and analysis methods,” *IMAC: Conference and Exposition on Structural Dynamics*, pages 437–443.
- [17] Goodding J, Griffiee JC, Ardelean EV (2008) “Parameter estimation and structural dynamics modeling of electrical cable harnesses on precision structures,” *49th AIAA/ASME/ASCE/AHS/ASC Structures, Structural Dynamics, and Materials Conference, 16th AIAA/ASME/AHS Adaptive Structures Conference, 10th AIAA Non-Deterministic Approaches Conference, 9th AIAA Gossamer Spacecraft Forum, 4th AIAA Multidisciplinary Design Optimization Specialists Conference*, page 1852. doi:10.2514/6.2008-1852
- [18] Nashif AD, Jones DI, Henderson JP (1985) *Vibration Damping*, John Wiley & Sons.
- [19] Adhikari S, Woodhouse J (2001) “Identification of damping: Part 1, viscous damping,” *Journal of Sound and Vibration* 243 (1): 43–61. doi:10.1006/jsvi.2000.3391
- [20] Banks HT, Inman DJ (1989) “On damping mechanisms in beams,” Technical report Institute for Computer Application in Science and Engineering.
- [21] Edem IB (2006) “The exact two-node timoshenko beam finite element using analytical bending and shear rotation interdependent shape functions,” *International Journal for Computational Methods in Engineering Science and Mechanics* 7: 425–431. doi:10.1080/15502280600826381
- [22] Bazoune A, Khulief YA (2003) “Shape functions of three-dimensional timoshenko beam element,” *Journal of Sound and Vibration* 259 (2): 473–480. doi:10.1006/jsvi.2002.5122
- [23] Friedman Z, Kosmatka JB (1993) “An improved two-node timoshenko beam finite element,” *Computers and Structures* 47 (3): 473–481. doi:10.1016/0045-7949(93)90243-7

- [24] Kosmatka JB (1995) “An improved two-node finite element for stability and natural frequencies of axial-loaded timoshenko beams,” *Computers and Structures* 57 (1): 141–149. doi:10.1016/0045-7949(94)00595-T
- [25] Thomas DL, Wilson JM, Wilson RR (1973) “Timoshenko beam finite elements,” *Journal of Sound and Vibration* 31 (3): 315–330. doi:10.1016/S0022-460X(73)80276-7
- [26] Thomas J, Abbas BAH (1975) “Finite element model for dynamic analysis of timoshenko beam,” *Journal of Sound and Vibration* 41 (3): 291–299. doi:10.1016/S0022-460X(75)80176-3
- [27] Wang C, Reddy JN, Lee K (2000) *Shear deformable beams and plates: Relationships with classical solutions*, Elsevier.